

CHEMISTRY

A **European** Journal

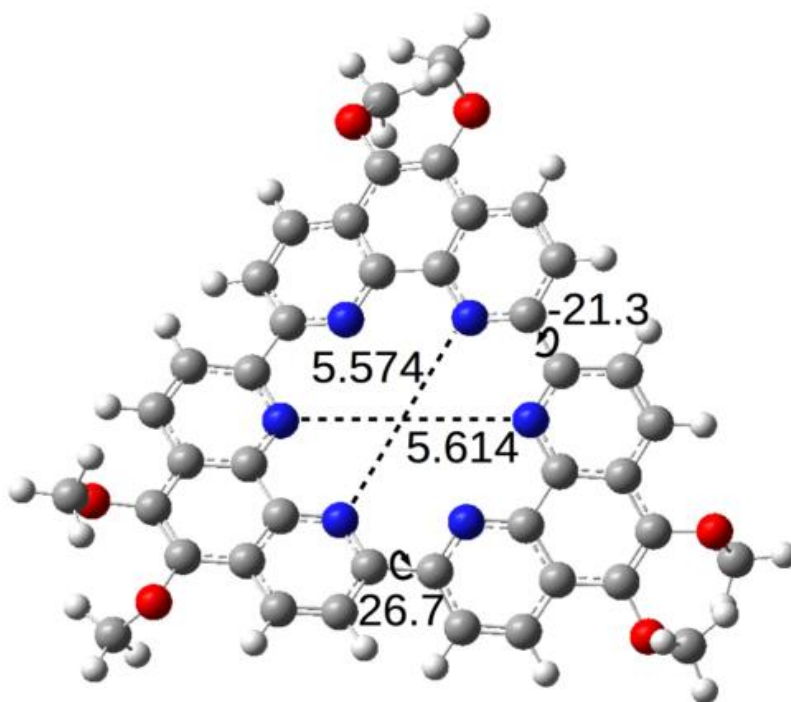
Supporting Information

Torands Revisited: Metal Sequestration and Self-Assembly of Cyclo-2,9-tris-1,10-phenanthroline Hexaaza Macrocycles

Matthias Georg Schwab,^[a, f] Masayoshi Takase,^[b] Alexey Mavrinsky,^[a] Wojciech Pisula,^[a] Xinliang Feng,^[a] José A. Gámez,^[c] Walter Thiel,^[d] Kunal S. Mali,^[e] Steven de Feyter,^[e] and Klaus Müllen^{*[a]}

chem_201406602_sm_miscellaneous_information.pdf

**Torands Revisited –
Metal Sequestration and Self-Assembly of
Cyclo-2,9-tris-1,10-phenanthroline
Hexaaza Macrocycles**



Materials and methods

Chemicals and Solvents

All chemicals and solvents used were obtained from the companies ABCR, Acros, Aldrich, Merck and Strem. Unless otherwise mentioned, they were used as obtained.

Chromatography

Preparative column chromatography was performed on silica gel from Merck with a grain size of 63.0 - 200.0 μm (silica gel) or 40.0 - 63.0 μm (flash silica gel).

For analytical thin layer chromatography (TLC), silica gel coated substrates (60 F254) from Merck were used. Compounds were detected by fluorescence quenching at 254 nm, self-fluorescence at 366 nm or staining in an iodine vapor chamber. For eluents, analytically pure solvents were used.

Recycling gel permeation chromatography (rGPC) was performed on a JAI LC-9101 equipped with JAI PS GPC columns using chloroform as eluent at room temperature.

NMR Spectroscopy

^1H -NMR, ^{13}C -NMR, and C,H-COSY experiments were recorded in the listed deuterated solvents on a Bruker DPX 250, Bruker DRX 500 or a Bruker DRX 700 spectrometer. The deuterated solvent was used as an internal standard,

Mass Spectrometry (MS/MALDI-TOF)

Field-desorption mass spectra were obtained on a VG Instruments ZAB 2-SE-FPD spectrometer. MALDI-TOF spectrometry was conducted on a Bruker Reflex II-TOF spectrometer, utilizing a 337 nm nitrogen laser. If not specifically mentioned, tetracyanoquinodimethane (TCNQ) was used as the matrix substance for solid state preparation. Else, the samples were directly measured from chloroform or THF by drop-casting the solution on the sample holder.

Elemental Combustion Analysis (ECA)

Elemental analysis of solid samples was carried out on a Foss Heraeus Vario EL. All samples were exhaustively dried under high vacuum prior to the analysis in order to remove possible remains of solvents and humidity

UV/VIS spectra were measured on a Perkin-Elmer Lambda 9 spectrophotometer at room temperature.

Optical Spectroscopy

Solution UV-vis spectra were recorded at room temperature on a Perkin-Elmer Lambda 100 spectrophotometer. Solvents of spectroscopic grade were employed. The baseline was corrected by subtracting a measurement of the cuvette filled with pure solvent used for the measurement. Solution photoluminescence spectra were recorded at room temperature on a SPEX-Fluorolog II (212) spectrometer.

Two-Dimensional Wide-Angle X-Ray Scattering (2D-WAXS)

The two-dimensional wide-angle X-ray diffraction experiments of orientated filaments were performed by means of a rotating anode (Rigaku 18 kW) X-ray beam with a pinhole collimation and a 2D Siemens detector with a beam diameter of 1.0 mm. A double graphite monochromator for the Cu-K α radiation ($\lambda = 0.154$ nm) was used. The patterns were recorded with vertical orientation of the filament axis and with the beam perpendicular to the filament.

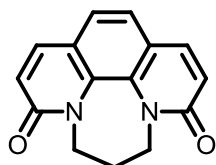
Single Crystal X-Ray Analysis

The single crystal analysis was performed on a Nonius-KCCD diffractometer with a Mo-K α ($\lambda = 0.072$ nm, graphite monochromatized) at a temperature of 150 K. The structures were solved by direct methods (Shelxs) and refined with anisotropic temperature factors for all non-hydrogen atoms. The hydrogen atoms were refined with fixed isotropic temperature factors in the riding mode.

¹³C-NMR (75 MHz, D₂O): δ 164.23, 150.85, 147.33, 134.09, 130.23, 127.30, 60.37, 30.89.

Elemental Analysis: found 46.40 % C, 3.75 % H, 7.45 % N - calc. 47.15 % C, 3.69 % H, 7.33 % N.

6,7-Dihydro-3H-[1,4]diazepino[1,2,3,4-Imn][1,10]phen-anthrolin-3,9(5H)-dione (**3**)^[1]



70.82 g (210.78 mmol) of potassium ferricyanide and 32.35 g (0.79 mol) of sodium hydroxide were mixed with 120.0 ml of H₂O after what the resulting red-brown suspension was cooled to 0 °C. 9.00 g (23.55 mmol) of **2** suspended in 80.0 ml of water were added drop-wise under continuous stirring keeping the temperature of the mixture below 5 °C. After 2 h, the reaction mixture was carefully neutralized with concentrated hydrochloric acid and the resulting precipitate was collected. The aqueous phase was removed under reduced pressure. The inorganic residue was extracted with THF for 72 h to yield in total 2.44 g (9.66 mmol) of **3** as a yellow powder in 41 %.

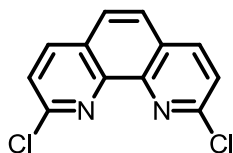
¹H-NMR (250 MHz, CD₂Cl₂): δ 7.72 (d, J = 9.5, 2H), 7.36 (s, 2H), 6.73 (d, J = 9.4 Hz, 2H), 4.27 (t, J = 6.4, 4H), 2.38 (p, J = 6.6, 2H).

¹³C-NMR (75 MHz, CD₂Cl₂): δ 162.94, 139.27, 132.78, 123.46, 123.34, 123.09, 46.07, 26.30.

MS (FD, 8kV): m/z (%) = 252.8 (100.0 %, M⁺), (calc. C₁₅H₁₂N₂O₂ = 252.27 g/mol).

Elemental Analysis: found 66.98 % C, 4.94 % H, 11.24 % N - calc. 71.42 % C, 4.79 % H, 11.10 % N.

2,9-Dichloro-1,10-phenanthroline (**4**)^[1]



1.50 g (5.95 mmol) of **3** and 2.65 g (12.73 mmol) of phosphorus pentachloride were dispersed in 18.0 ml of phosphoryl chloride. The turbid mixture was heated to reflux for 8 h to yield a brown solution. After cooling, the reaction mixture was slowly added to 150.0 ml of an acidified ice/water mixture. After complete hydrolysis, the aqueous phase was brought to pH = 14 by slow addition of NaOH. The resulting precipitate was collected and the aqueous

phase extracted several times with DCM. The crude product was purified by column chromatography (ethyl acetate/hexane = 1/1) to yield 1.19 g (4.78 mmol) of **4** as an off-white powder in 82 %.

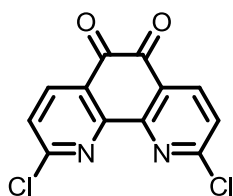
¹H-NMR (250 MHz, CD₂Cl₂): δ 8.26 (d, J = 8.4, 2H), 7.87 (s, 2H), 7.66 (d, J = 8.4, 2H).

¹³C-NMR (75 MHz, CD₂Cl₂): δ 151.90, 145.42, 139.54, 128.46, 126.84, 125.18.

MS (FD, 8kV): m/z (%) = 250.1 (100.0 %, M⁺), (calc. C₁₂H₆Cl₂N₂ = 249.10 g/mol).

Elemental Analysis: found 57.94 % C, 2.39 % H, 11.35 % N - calc. 57.86 % C, 2.43 % H, 11.25 % N.

2,9-Dichloro-1,10-phenanthrolin-5,6-dione (**5**)^[2]



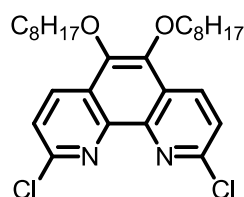
1.00 g (5.85 mmol) of **4** and 4.77 g (40.08 mmol) of potassium bromide were mixed and cooled in a flask with gas outlet to - 5 °C. 14.0 ml of concentrated H₂SO₄ were added slowly always keeping the temperature of the mixture below 0 °C. To the orange viscous mixture were slowly added 7.0 ml of concentrated nitric acid. Subsequently, the reaction mixture was heated to 80 °C for 3 h. Bromine vapours were passed through a 10 % solution of sodium thiosulfate. After cooling, the reaction mixture was added to 200.0 ml of an ice/water mixture and stirred for 2 h at room temperature. The yellow-orange precipitate was collected and washed with H₂O and treated with an aqueous solution of sodium thiosulfate. 1.43 g (5.15 mmol) of **5** were obtained and used for the next step without further purification (88 %).

¹H-NMR (250 MHz, CD₂Cl₂): δ 8.42 (d, J = 8.2, 2H), 7.63 (d, J = 8.2, 2H).

¹³C-NMR (75 MHz, CD₂Cl₂): δ 177.83, 159.06, 158.21, 152.76, 140.16, 127.70.

MS (FD, 8kV): m/z (%) = 278.8 (100.0 %, M⁺), (calc. C₁₂H₄Cl₂N₂O₂ = 279.08 g/mol).

2,9-Dichloro-5,6-bis(octyloxy)-1,10-phenanthroline (**6a**)



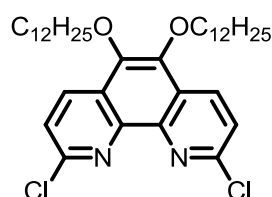
To a mixture of 10.0 ml water and 10.0 ml THF 0.50 g (1.81 mmol) of **5**, 0.38 g (1.17 mmol) tetra-*n*-butylammonium bromide and 1.89 g (10.83 mmol) sodium dithionite were added. Then, 1.15 g (6.00 mmol) octyl bromide was added to the mixture. A solution of 1.50 g (27.07 mmol) of potassium hydroxide in 10.0 ml water was subsequently added after what the reaction mixture turned black. The reaction mixture was stirred for 48 h at 40 °C. After dilution with water, the reaction mixture was extracted with ethyl acetate. The crude product was purified by column chromatography (DCM/ethyl acetate = 50:1) to yield 0.55 g (1.09 mmol) of **6a** in 60 % as a light yellow powder.

¹H-NMR (300 MHz, CD₂Cl₂): δ 8.53 (d, J = 8.6, 2H), 7.64 (d, J = 8.6, 2H), 4.23 (t, J = 6.7, 4H), 1.86 (p, J = 6.8, 2H), 1.62 - 1.22 (m, 20H), 0.88 (t, J = 6.9, 6H).

¹³C-NMR (75 MHz, CD₂Cl₂): δ 150.81, 143.21, 143.08, 134.30, 126.44, 124.93, 74.78, 32.40, 30.85, 29.99, 29.82, 26.69, 23.23, 14.43.

MS (FD, 8kV): m/z (%) = 503.8 (100.0 %, M⁺), (calc. C₂₈H₃₈Cl₂N₂O₂ = 505.52 g/mol).

2,9-Dichloro-5,6-bis(dodecyloxy)-1,10-phenanthroline (**6b**)



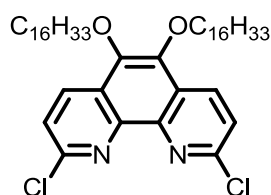
To a mixture of 10.0 ml water and 10.0 ml THF 1.00 g (3.61 mmol) of **5**, 0.75 g (2.33 mmol) tetra-*n*-butylammonium bromide and 3.77 g (21.66 mmol) sodium dithionite were added. Then, 3.0 g (12.0 mmol) dodecyl bromide was added to the mixture. A solution of 3.0 g (54.15 mmol) of potassium hydroxide in 20.0 ml water was subsequently added after what the reaction mixture turned black. The reaction mixture was stirred for 48 h at 40 °C. After dilution with water, the reaction mixture was extracted with ethyl acetate. The crude product was purified by column chromatography (DCM/ethyl acetate = 50:1) to yield 1.49 g (2.41 mmol) of **6b** in 67 % as a light yellow powder.

¹H-NMR (250 MHz, CD₂Cl₂): δ = 8.53 (d, J = 8.6, 2H), 7.64 (d, J = 8.6, 2H), 4.22 (t, J = 6.7, 4H), 1.86 (p, J = 7.0, 4H), 1.61 - 1.10 (m, 36H), 0.87 (t, J = 6.9, 6H).

¹³C-NMR (75 MHz, CD₂Cl₂): δ 150.79, 143.19, 143.07, 134.27, 126.41, 124.91, 74.76, 32.51, 30.86, 30.27, 30.24, 30.21, 30.19, 30.05, 29.95, 26.71, 23.28, 14.46.

MS (FD, 8kV): m/z (%) = 616.1 (100.0 %, M⁺), (calc. C₃₆H₅₄Cl₂N₂O₂ = 617.73 g/mol).

2,9-Dichloro-5,6-bis(hexadecyloxy)-1,10-phenanthroline (6c)



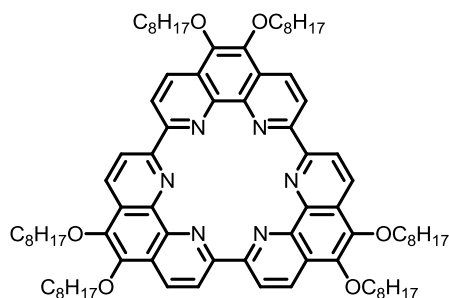
To a mixture of 8.0 ml water and 8.0 ml THF 0.40 g (1.43 mmol) of **5**, 0.30 g (0.93 mmol) tetra-*n*-butylammonium bromide and 1.50 g (8.60 mmol) sodium dithionite were added. Then, 1.46 g (4.76 mmol) hexadecyl bromide was added to the mixture. A solution of 1.19 g (21.50 mmol) of potassium hydroxide in 8.0 ml water was subsequently added after what the reaction mixture turned black. The reaction mixture was stirred for 48 h at 40 °C. After dilution with water, the reaction mixture was extracted with ethyl acetate. The crude product was purified by column chromatography (DCM/ethyl acetate = 50:1) to yield 0.71 g (0.97 mmol) of **6c** in 68 % as a light yellow powder.

¹H-NMR (300 MHz, CD₂Cl₂): δ 8.53 (d, J = 8.6, 2H), 7.64 (d, J = 8.6, 2H), 4.22 (t, J = 6.7, 4H), 1.88 (p, J = 7.0, 4H), 1.60 - 1.12 (m, 52H), 0.87 (t, J = 6.9, 6H).

¹³C-NMR (75 MHz, CD₂Cl₂): δ 150.81, 143.21, 143.09, 134.30, 126.43, 124.93, 74.78, 32.50, 30.85, 30.28, 30.25, 30.24, 30.20, 30.17, 30.03, 29.94, 26.69, 23.27, 14.45.

MS (FD, 8kV): m/z (%) = 728.0 (100.0 %, M⁺), (calc. C₄₄H₇₀Cl₂N₂O₂ = 729.94 g/mol).

Cyclo-2,9-tris-(5,6)-bis(octyloxy)-1,10-phenanthroline (7a)



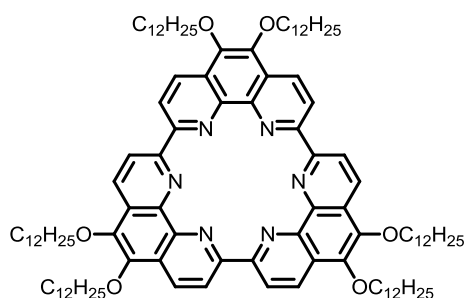
The catalyst solution was prepared inside the glove box by adding 12.0 ml DMF and 24.0 ml toluene to a mixture of 0.26 g (0.95 mmol) bis(cyclooctadiene)nickel(0), 0.15 g (0.95 mmol) 2,2'-bipyridine and 0.12 ml (0.95 mmol) cyclooctadiene. The resulting solution was stirred for 30 min at 60 °C. Then, a solution of 0.20 g (0.40 mmol) of **6a** in 12.0 ml toluene was added dropwise over 30 min. The reaction mixture was stirred for 72 h at 60 °C under the exclusion of light. After cooling, the mixture was diluted with diethyl ether and washed with diluted hydrochloric acid (2 M). The crude product was pre-purified by column chromatography on silica (DCM/methanol = 10/1). Further purification was achieved by preparative gel permeation chromatography (chloroform) to yield 28 mg (0.021 mmol) of **6a** in 16 % as an orange waxy solid.

¹H-NMR (500 MHz, CD₂Cl₂): δ 8.98 (d, J = 8.7, 6H), 8.75 (d, J = 8.8, 6H), 4.37 (t, J = 6.6, 12H), 1.98 (p, J = 7.0, 12H), 1.81 - 1.22 (m, 60H), 0.92 (t, J = 7.0, 18H).

¹³C-NMR (126 MHz, CD₂Cl₂): δ 153.58, 144.50, 143.36, 133.65, 128.21, 123.07, 74.96, 32.45, 30.96, 30.06, 29.89, 26.78, 23.27, 14.46.

MS (MALDI-TOF): m/z (%) = 1325.96 (100.0 %), 1326.96 (95.5 %), 1327.96 (49.4 %), 1328.26 (20.5 %), (calc. C₈₄H₁₁₄N₆NaO₆ = 1326.83 g/mol - isotop. distr.: 1325.87 (100.0 %), 1326.87 (93.3 %), 1327.88 (42.2 %), 1328.98 (20.9 %)).

Cyclo-2,9-tris-(5,6)-bisdodecyloxy-1,10-phenanthroline (**7b**)



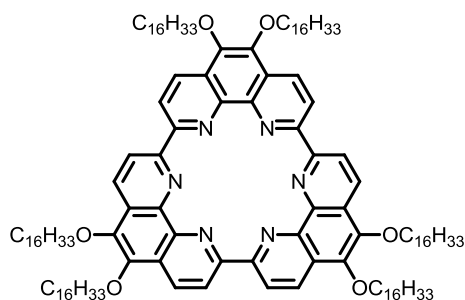
The catalyst solution was prepared inside the glove box by adding 20.0 ml DMF and 40.0 ml toluene to a mixture of 0.43 g (1.55 mmol) bis(cyclooctadiene)nickel(0), 0.24 g (1.55 mmol) bipyridine and 0.19 ml (1.55 mmol) cyclooctadiene. The resulting solution was stirred for 30 min at 60 °C. Then, a solution of 0.40 g (0.65 mmol) of **6b** in 20.0 ml toluene was added dropwise over 30 min. The reaction mixture was stirred for 72 h at 60 °C under the exclusion of light. After cooling, the mixture was diluted with diethyl ether and washed with diluted hydrochloric acid (2 M). The crude product was pre-purified by column chromatography on silica (DCM/methanol = 10/1). Further purification was achieved by preparative gel permeation chromatography (chloroform) to yield 67 mg (0.041 mmol) of **7b** in 19 % as an orange waxy solid.

¹H-NMR (500 MHz, CD₂Cl₂): δ 8.98 (d, J = 8.7, 6H), 8.79 (d, J = 8.8, 6H), 4.37 (t, J = 6.6, 12H), 1.86 (p, J = 7.0, 12H), 1.75 - 1.10 (m, 108H), 0.89 (t, J = 6.9, 18H).

¹³C-NMR (126 MHz, CD₂Cl₂): δ 153.81, 144.63, 143.01, 133.20, 127.53, 123.01, 74.91, 32.56, 31.11, 30.37, 30.34, 30.24, 30.01, 26.89, 23.31, 14.47.

MS (MALDI-TOF): m/z (%) = 1663.24 (100.0 %), 1662.25 (82.3 %), 1664.25 (62.4 %), 1665.26 (29.5 %), (calc. C₁₀₈H₁₆₂N₆NaO₆ = 1663.47 g/mol - isotop. distr.: 1663.25 (100.0 %), 1662.25 (84.1%), 1664.25 (62.2 %), 1665.26 (22.9 %)).

Cyclo-2,9-tris-(5,6)-bishexadecyloxy-1,10-phenanthroline (**7c**)



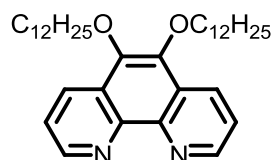
The catalyst solution was prepared inside the glove box by adding 10.0 ml DMF and 20.0 ml toluene to a mixture of 0.23 g (0.82 mmol) bis(cyclooctadiene)nickel(0), 0.13 g (0.82 mmol) bipyridine and 0.10 ml (0.82 mmol) cyclooctadiene. The resulting solution was stirred for 30 min at 60 °C. Then, a solution of 0.25 g (0.34 mmol) of **6c** in 10.0 ml toluene was added dropwise over 30 min. The reaction mixture was stirred for 72 h at 60 °C under the exclusion of light. After cooling, the mixture was diluted with diethyl ether and washed with diluted hydrochloric acid (2 M). The crude product was pre-purified by column chromatography on silica (DCM/methanol = 10/1). Further purification was achieved by preparative gel permeation chromatography (chloroform) to yield 27 mg (0.041 mmol) of **7c** in 12 % as an orange waxy solid.

¹H-NMR (500 MHz, CD₂Cl₂): δ 8.98 (d, J = 8.6, 6H), 8.76 (d, J = 8.8, 6H), 4.33 (t, J = 6.6, 12H), 1.98 (p, J = 7.0, 12H), 1.84 - 1.05 (m, 156H), 0.88 (t, J = 6.9, 18H).

¹³C-NMR (126 MHz, CD₂Cl₂): δ 153.77, 144.59, 143.37, 133.73, 128.21, 123.11, 74.97, 32.51, 30.97, 30.32, 30.27, 30.13, 29.95, 26.80, 23.27, 14.45.

MS (MALDI-TOF): m/z (%) = 1999.02 (100.0 %), 2000.02 (73.5 %), 1999.02 (72.5 %), 2001.02 (46.0 %), (calc. C₁₃₂H₂₁₀N₆NaO₆ = 2000.11 g/mol - isotop. distr.: 1999.62 (100.0 %), 2000.63 (73.2 %), 1998.62 (69.0 %), 2001.63 (35.8 %), 2002.63 (13.1 %)).

5,6-Bis(dodecyloxy)-1,10-phenanthroline (**9**)



To a mixture of 13.0 ml water and 13.0 ml THF 0.50 g (2.38 mmol) of 1,10-phenanthroline-5,6-dione **8**, 0.49 g (1.54 mmol) tetra-*n*-butylammonium bromide and 2.48 g (14.27 mmol) sodium dithionite were added. Then, 1.98 g (7.91 mmol) dodecyl bromide was added to the

mixture. A solution of 1.98 g (35.68 mmol) of potassium hydroxide in 13.0 ml water was subsequently added after what the reaction mixture turned deep red. The reaction mixture was stirred for 48 h at 40 °C. After dilution with water, the reaction mixture was extracted with ethyl acetate. The crude product was purified by column chromatography (DCM/ethyl acetate = 50:1) to yield 0.49 g (0.91 mmol) of **9** in 59 % as a light yellow powder.

¹H-NMR (250 MHz, CD₂Cl₂): δ 9.04 (dd, J = 1.7, 4.3, 2H), 8.57 (d, J = 8.3, 2H), 7.71 (dd, J = 4.3, 8.3, 2H), 4.23 (t, J = 6.7, 4H), 1.89 (p, J = 6.8, 4H), 1.61 - 1.10 (m, 36H), 0.88 (t, J = 6.6, 6H).

¹³C-NMR (75 MHz, CD₂Cl₂): δ 149.41, 144.98, 142.84, 130.77, 127.01, 123.35, 74.52, 32.52, 30.96, 30.66, 30.27, 30.24, 30.22, 30.09, 29.95, 26.78, 23.28, 14.45.

MS (FD, 8kV): m/z (%) = 548.1 (100.0 %, M⁺), (calc. C₃₆H₅₆N₂O₂ = 548.84 g/mol).

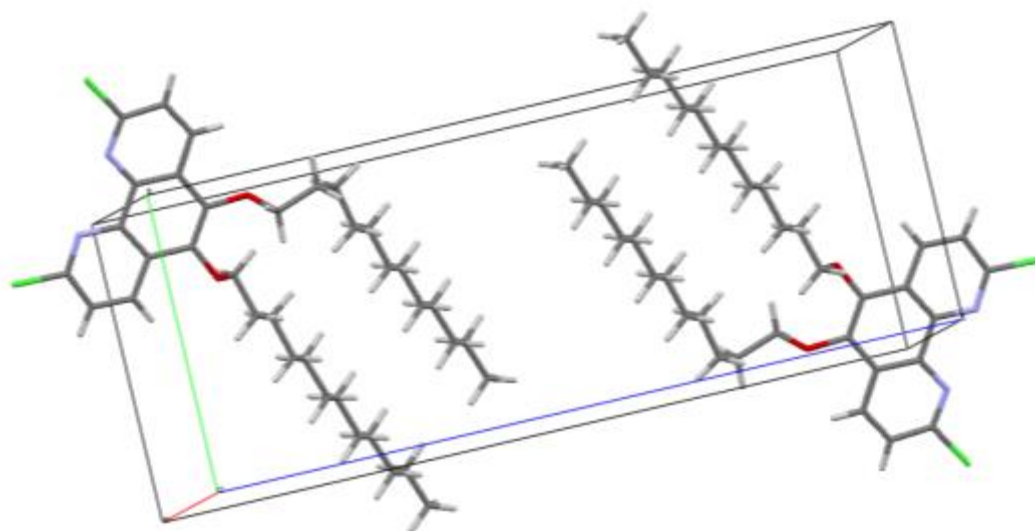
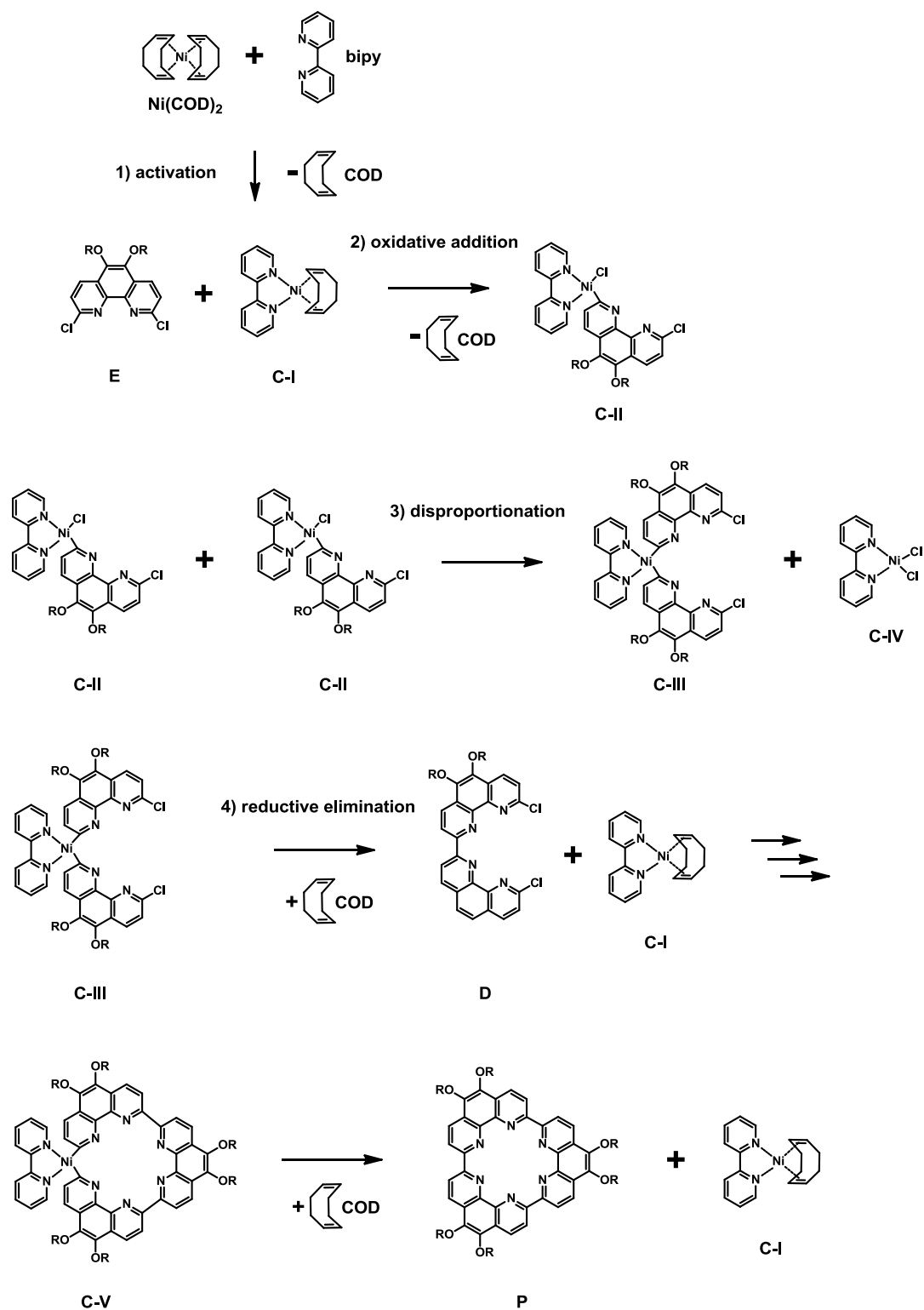


Fig. S1: Crystal structure of 2,9-dichloro-5,6-bis(dodecyloxy)-1,10-phenanthroline **6b**.

Proposed Reaction Mechanism during Formation of the Cyclo-2,9-tris-1,10-phenanthroline Macrocycle

The proposed mechanism towards the formation of the cyclo-2,9-tris-1,10-phenanthroline system relies on the fundamental reaction steps of organometallic chemistry and is shown in Scheme S2.^[3, 4]

The activation of the zerovalent nickel catalyst bis(cyclooctadiene)nickel(0) (**Ni(COD)₂**) is achieved *via* the replacement of one 1,5-cyclooctadiene (**COD**) ligand by the auxiliary ligand 2,2'-bipyridine (**bipy**). In the next step, oxidative addition of the 1,10-phenanthroline unit (**E**) to the activated complex **C-I** results in the insertion of the nickel atom into the carbon-chlorine bond leading to the formation of Ni(II) complex **C-II**.^[5-7] Two of these species disproportionate to yield the complex **C-III** in which the two aryl units are already brought into close proximity.^[6] The formation of complex **C-IV** in stoichiometric amounts is the reason for the consumption of the catalyst during the course of the reaction as this species further degrades to nickel(II) chloride. The subsequent reductive elimination of complex **C-III** yields the desired coupling product (**D**) and at the same time liberates the activated complex **C-I** that re-enters the catalytic cycle. For the formation of the open trimeric 1,10-phenanthroline species an analogous *intermolecular* reaction sequence involving the monomer and dimer can be expected. For the last step of the cyclotrimerization (closure of the open trimer to the final macrocycle) an *intramolecular* coupling is necessary. Once the trimer is coordinated to the metal centre, its rigid molecular backbone along with the ideal binding angles of 120 ° assists in the coordination of its second end to the same nickel site. Already **C-V** contains the predefined shape of the final product which is induced by the geometry of the complex. The macrocycle as the final reaction product (**P**) is then formed upon reductive elimination.



Scheme S2: Proposed reaction mechanism during the formation of the cyclo-2,9-tris-1,10-phenanthroline macrocycles involving *inter*- and *intramolecular* coupling steps.

NMR Analysis

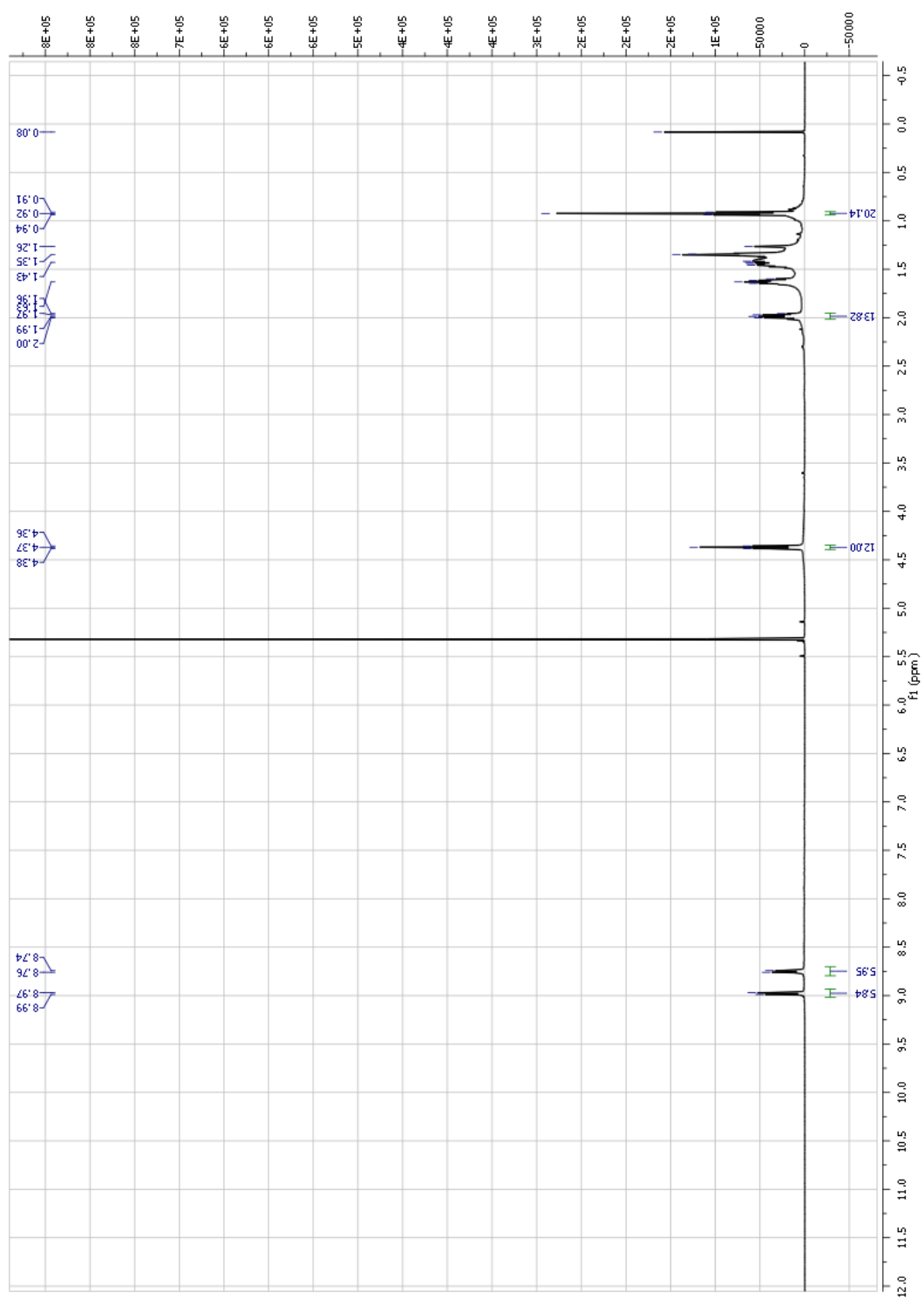


Fig. S2: ^1H NMR spectrum of **7a** in DCM-d_2 at $25\text{ }^\circ\text{C}$.

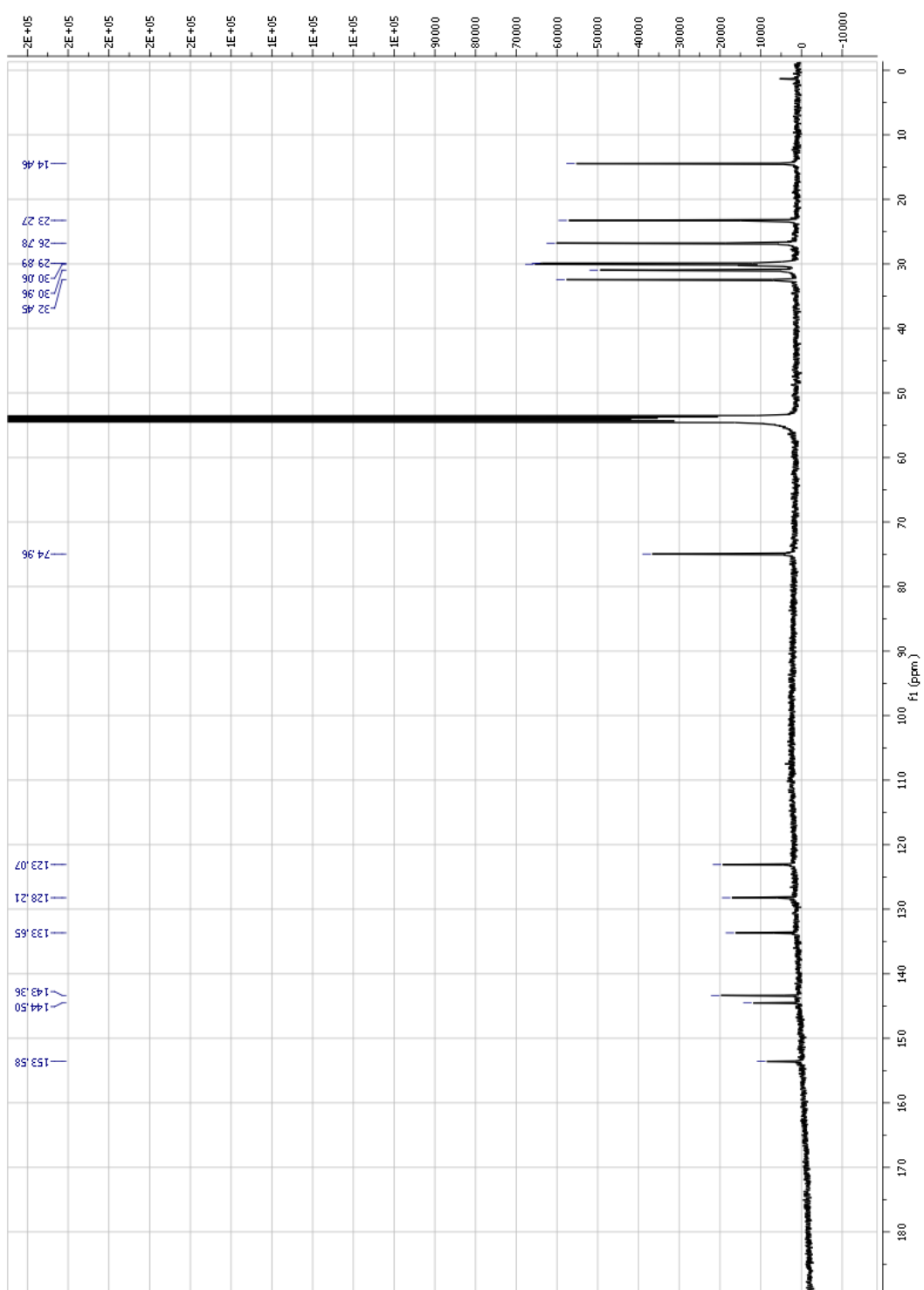


Fig. S3: ^{13}C NMR (CD_2Cl_2 , 126 MHz) spectrum of 7a-Na.

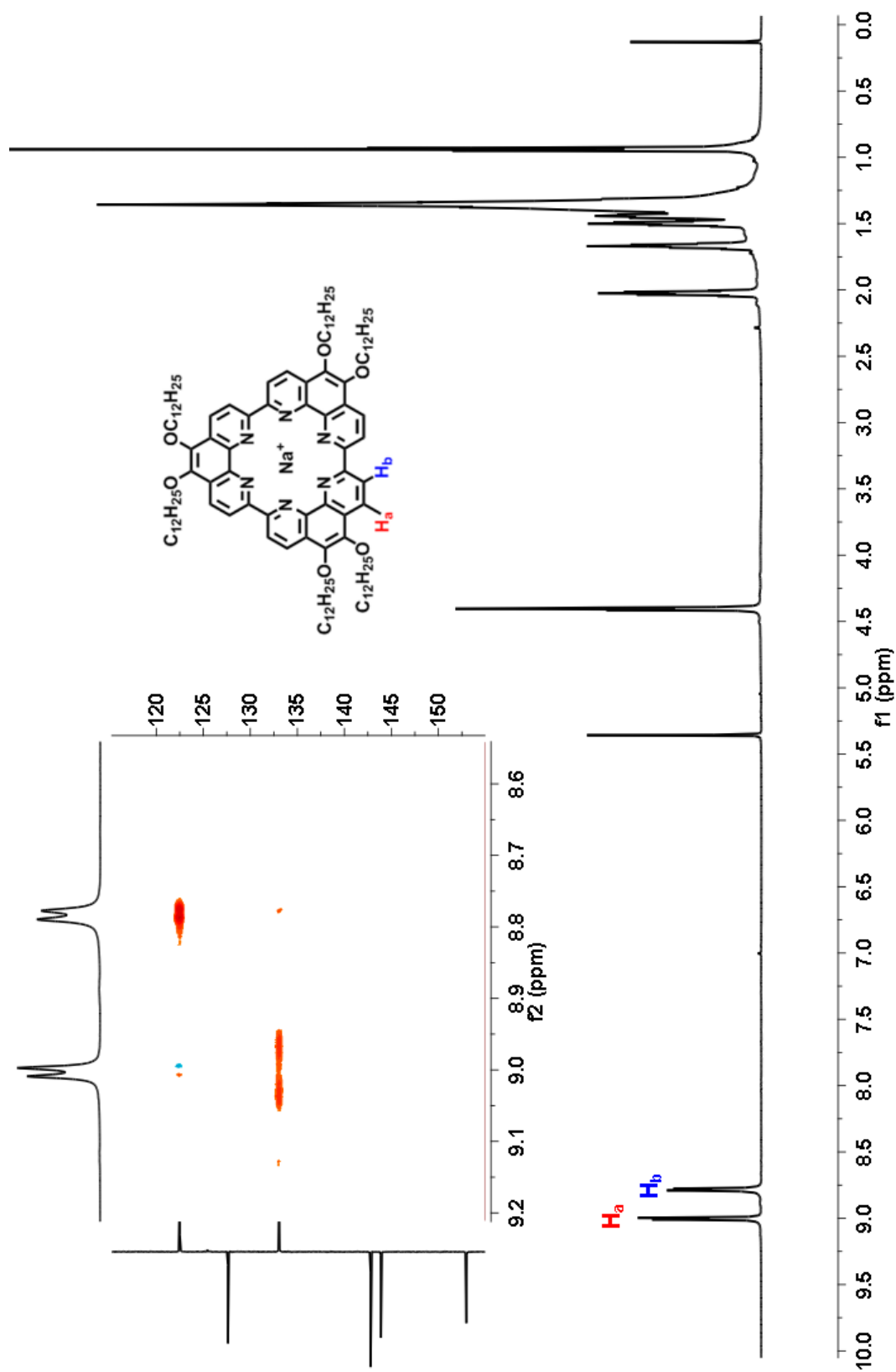


Fig. S4: ^1H NMR spectrum of **7b-Na** in DCM-d_2 at 25°C . The inset shows the $^1\text{H},^{13}\text{C}$ -COSY NMR spectrum of the aromatic region of the compound.

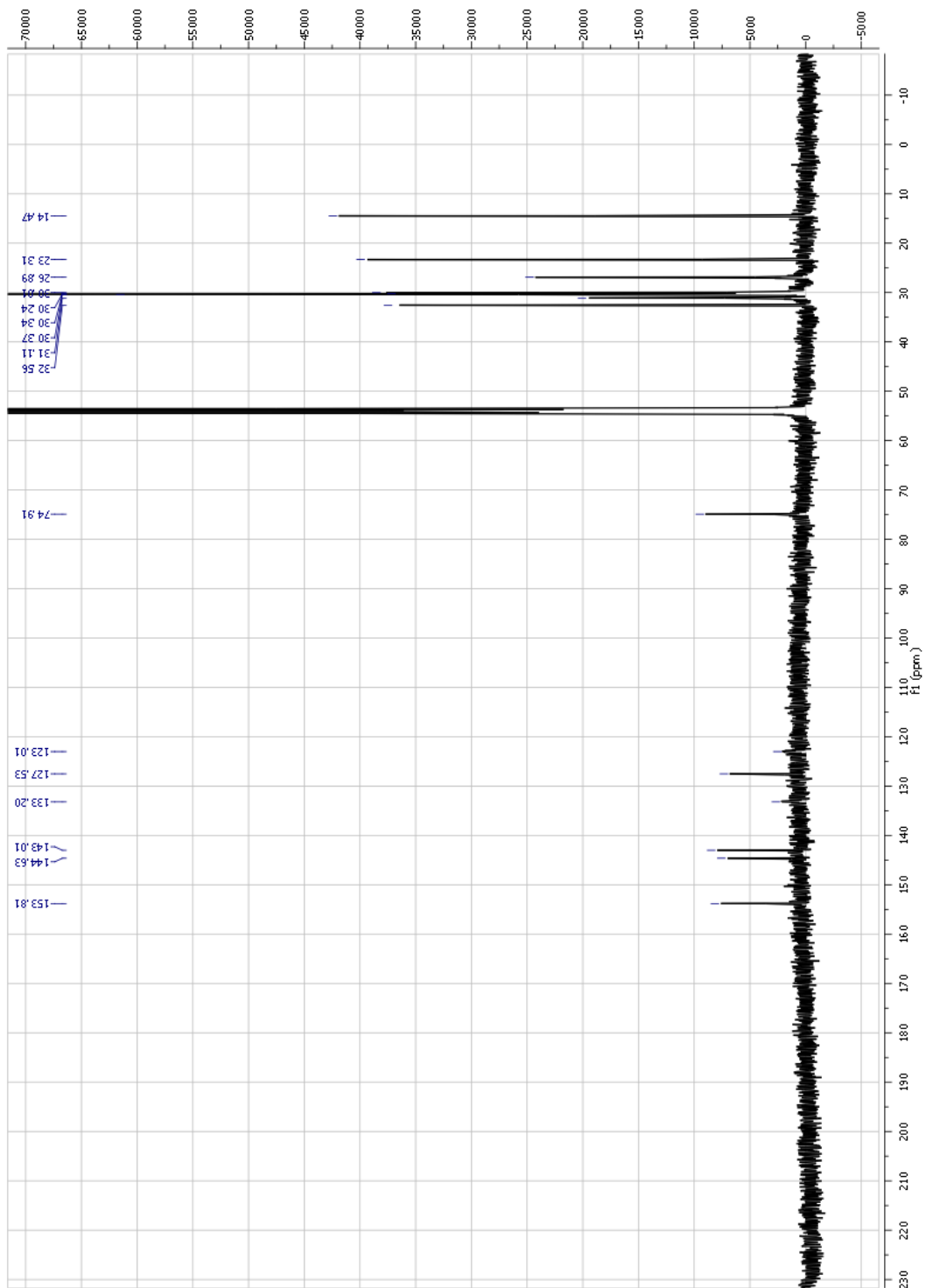


Fig. S5: ^{13}C NMR (CD_2Cl_2 , 126 MHz) spectrum of **7b-Na**.

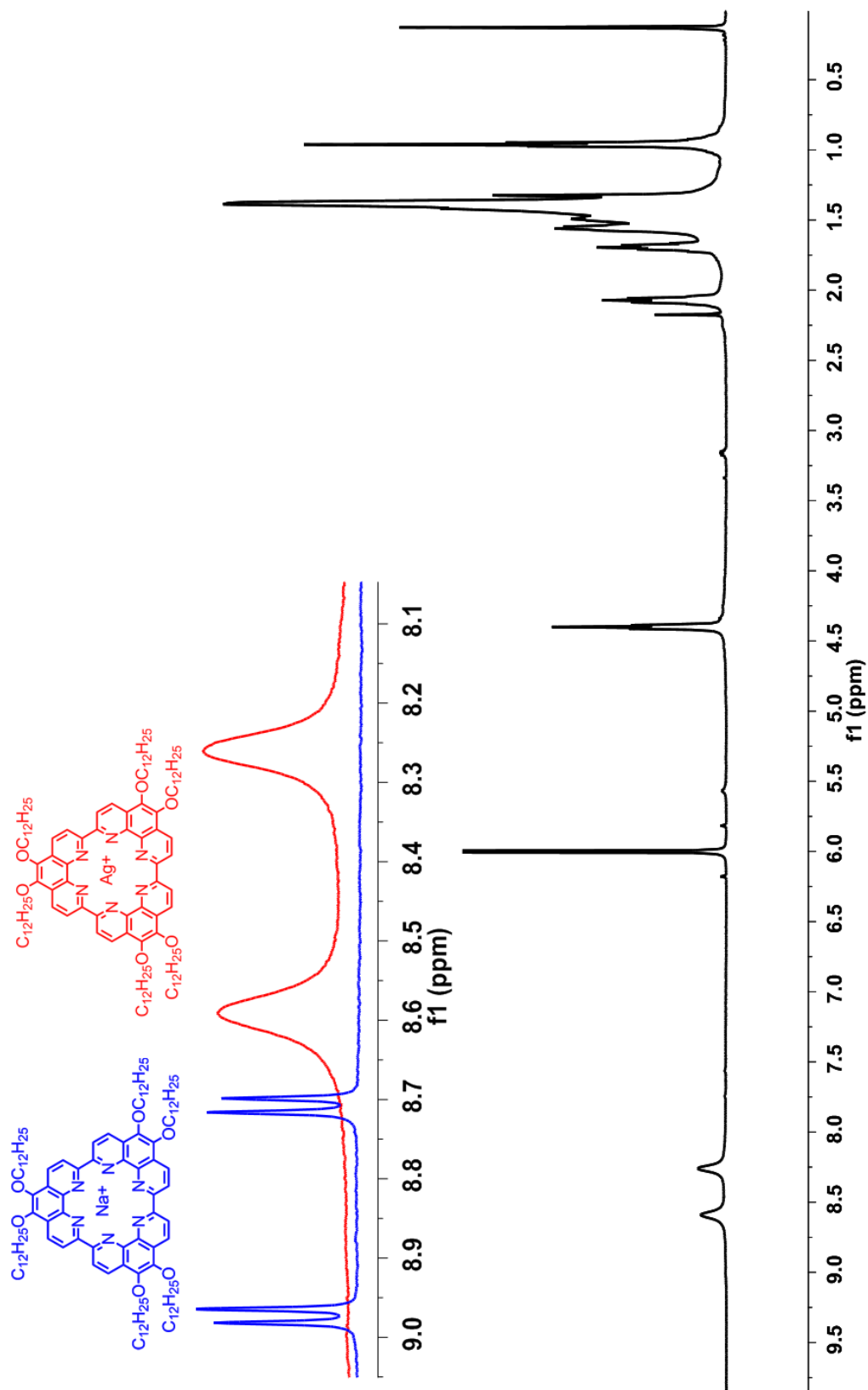


Fig.S6: ¹H NMR spectrum of **7b-Ag** in TCE-d₂. The inset shows a comparison between the aromatic region of parent **7b-Na** and **7b-Ag**.

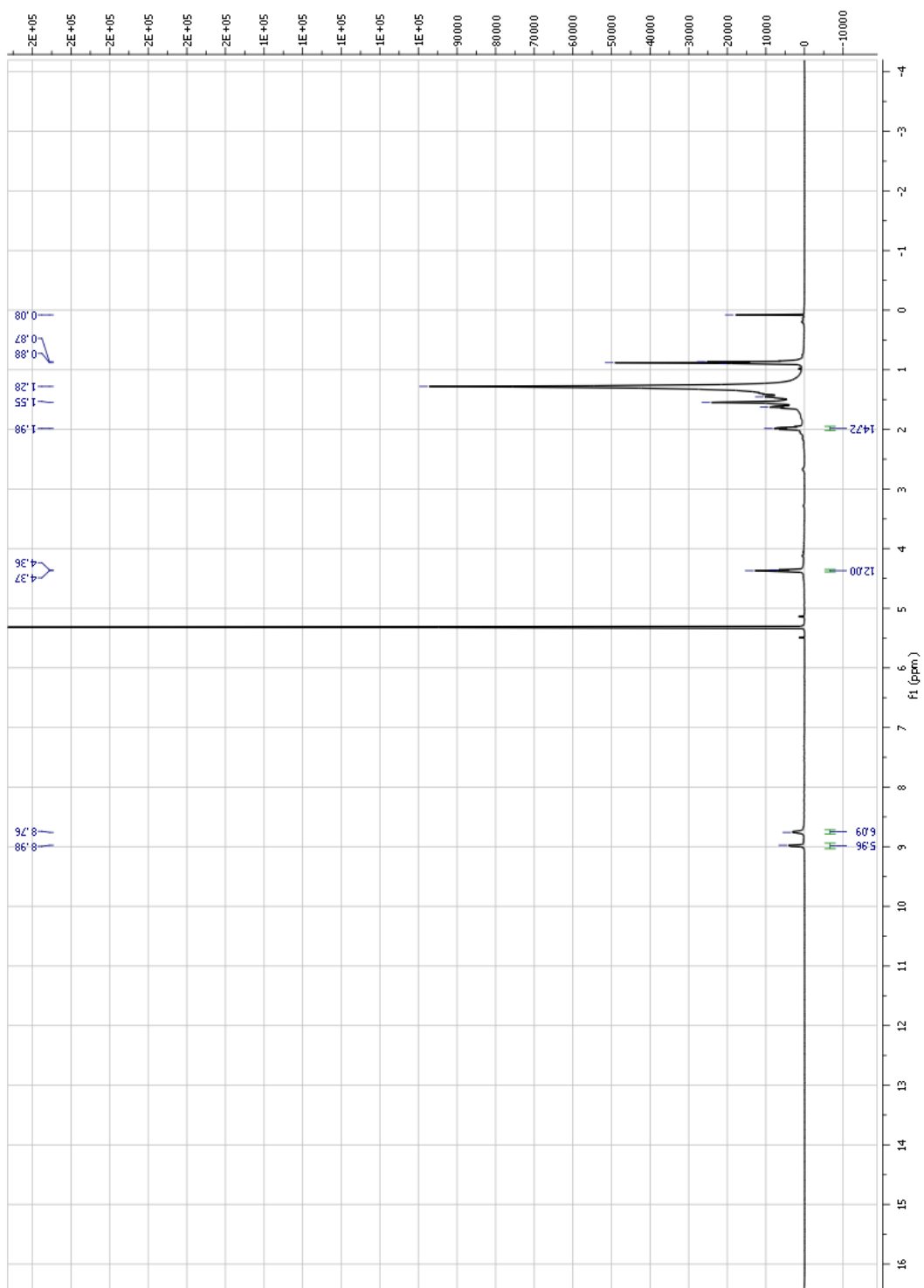


Fig.S7: ^1H NMR (CD_2Cl_2 , 500 MHz) spectrum of **7c-Na**.

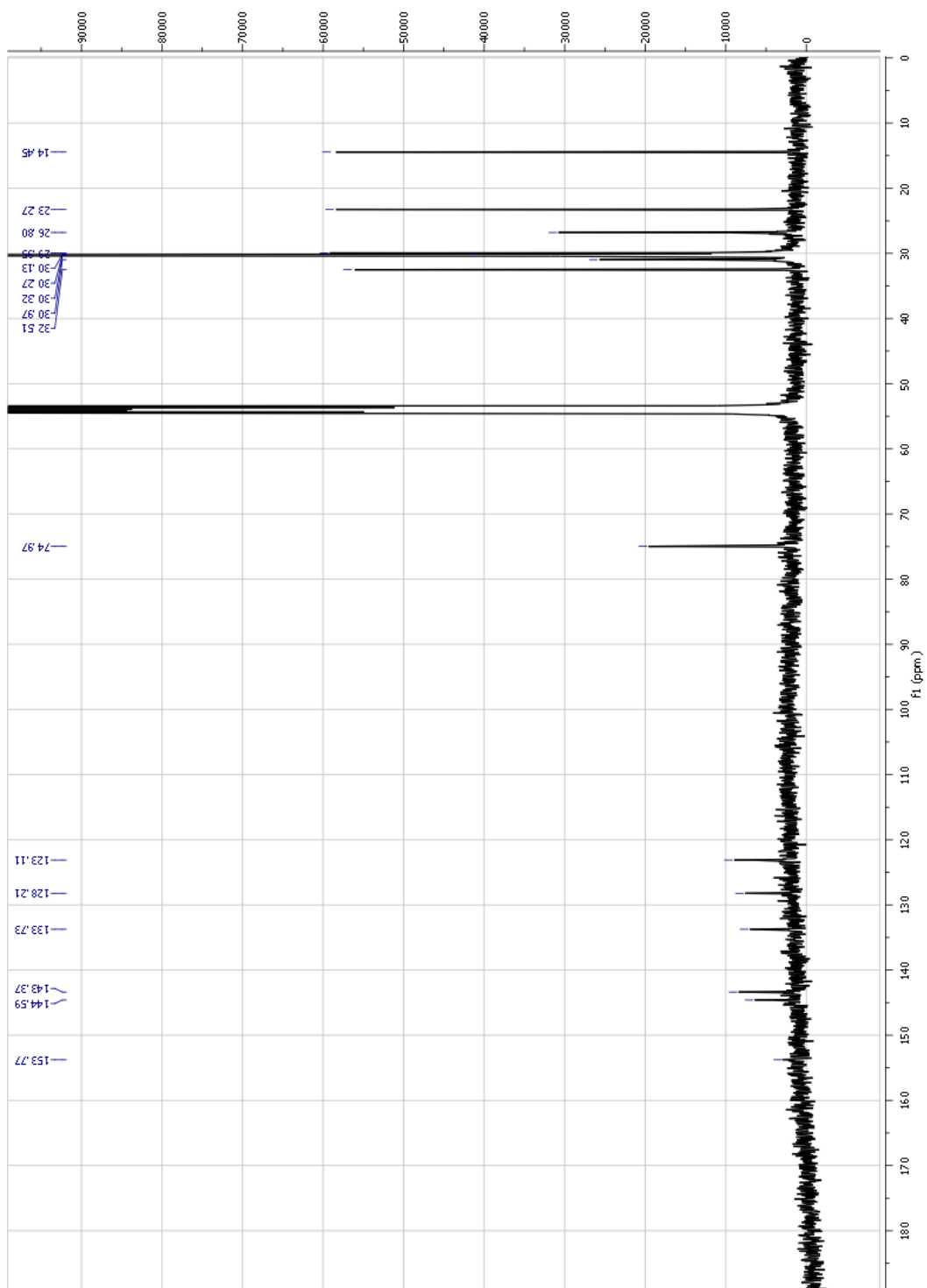


Fig.S8: ^{13}C NMR (CD_2Cl_2 , 126 MHz) spectrum of **7c-Na**.

MALDI-TOF Analysis

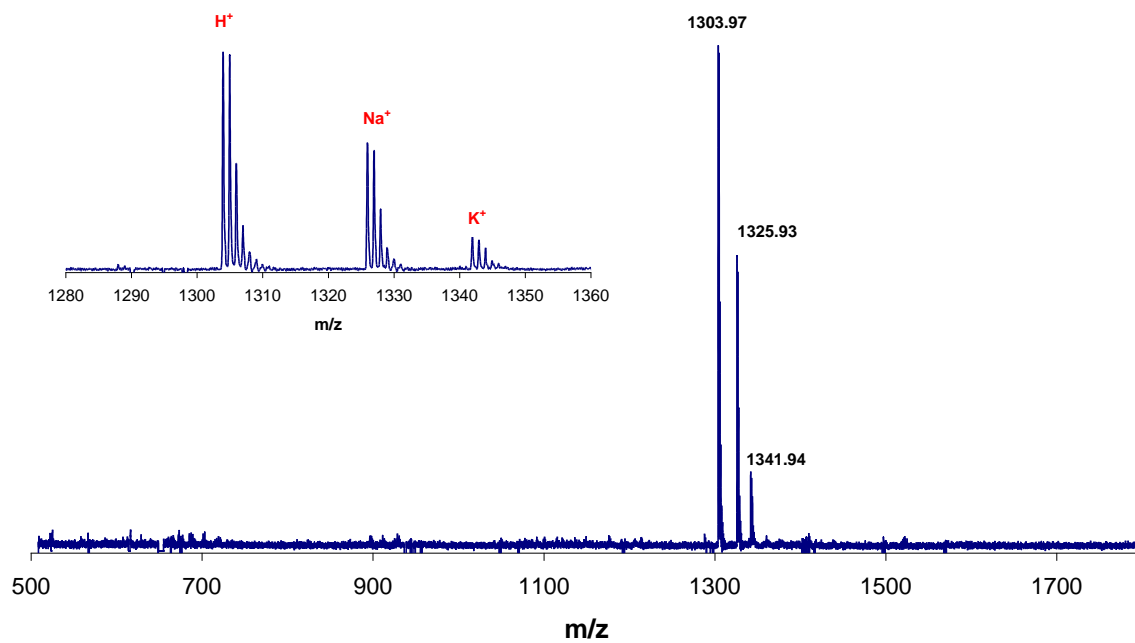


Fig. S9: MALDI-TOF spectrum of as-synthesized **7a**.

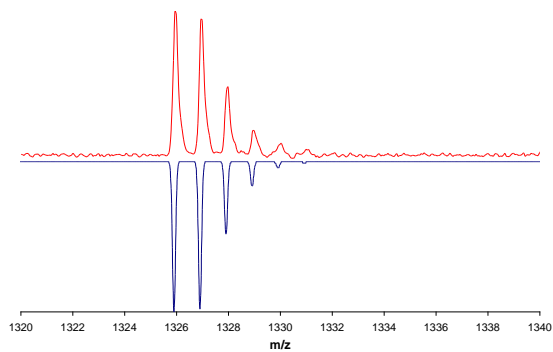


Fig.S10: Comparison between experimental (red) and theoretically calculated (blue) isotopic pattern of **7a-Na**.

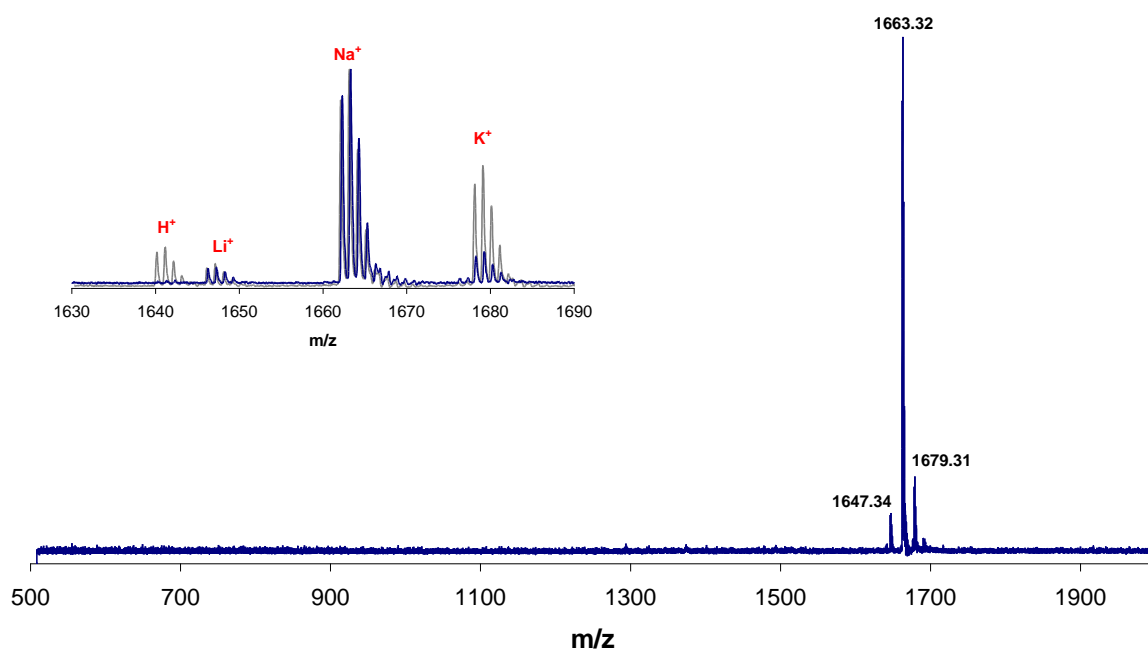


Fig.S11: MALDI-TOF spectrum of **7b-Na**; the inset shows the distribution of protonated macrocycle and its sodium and potassium complex before (gray) and after (blue) exposure to 2 M NaOH.

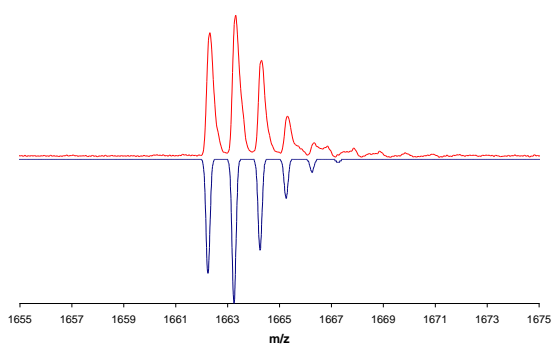


Fig.S12: Comparison between experimental (red) and theoretically calculated (blue) isotopic pattern of **7b-Na**.

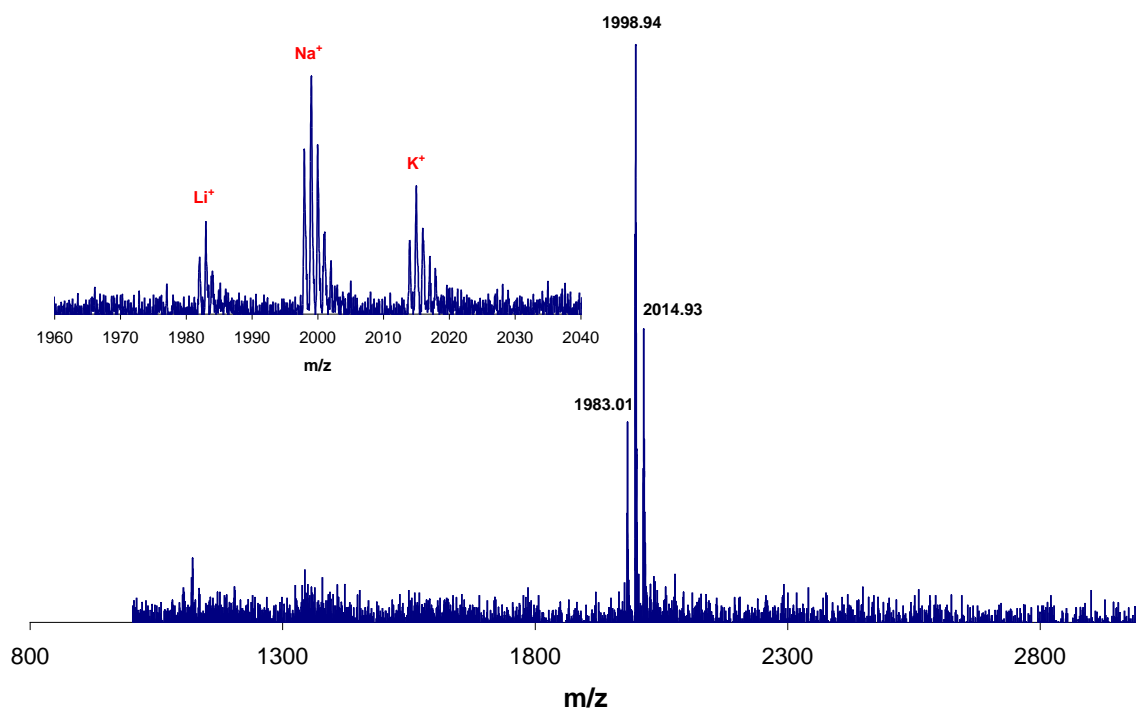


Fig.S13: MALDI-TOF spectrum of as-synthesized **7c**.

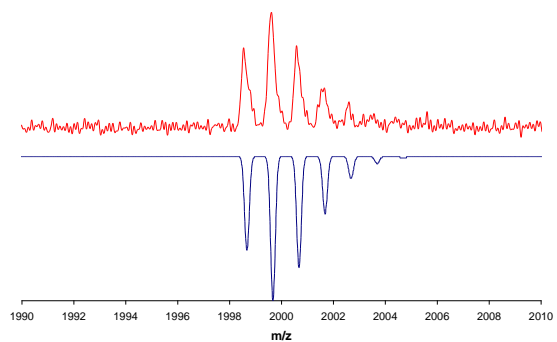


Fig.S14: Comparison between experimental (red) and theoretically calculated (blue) isotopic pattern of **7c-Na**.

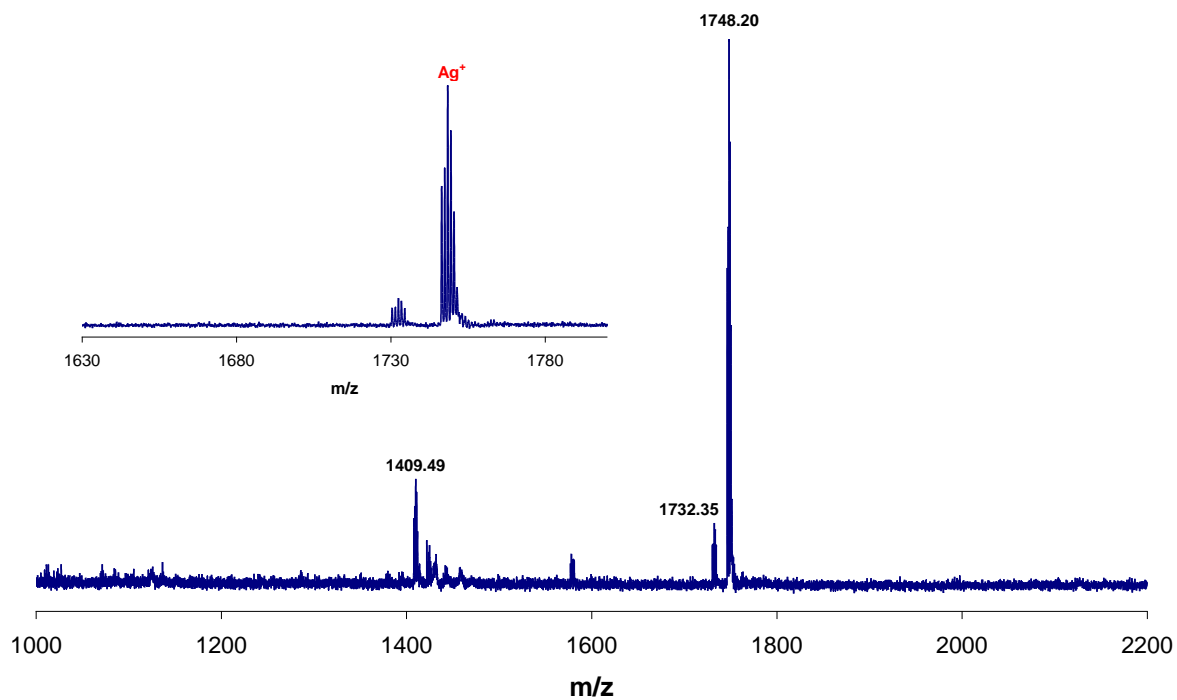


Fig.S15: MALDI-TOF spectrum of **7b** after mixing with Ag(OTf) in DCM/methanol.

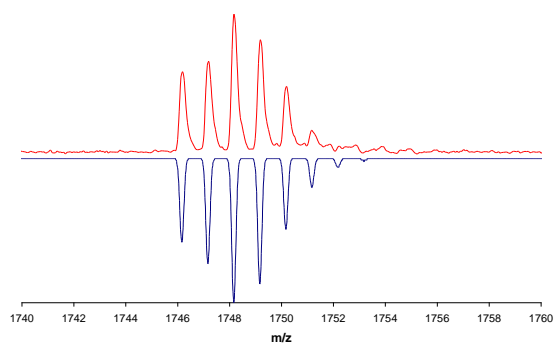


Fig.S16: Comparison between experimental (red) and theoretically calculated (blue) isotopic pattern of **7b-Ag**.

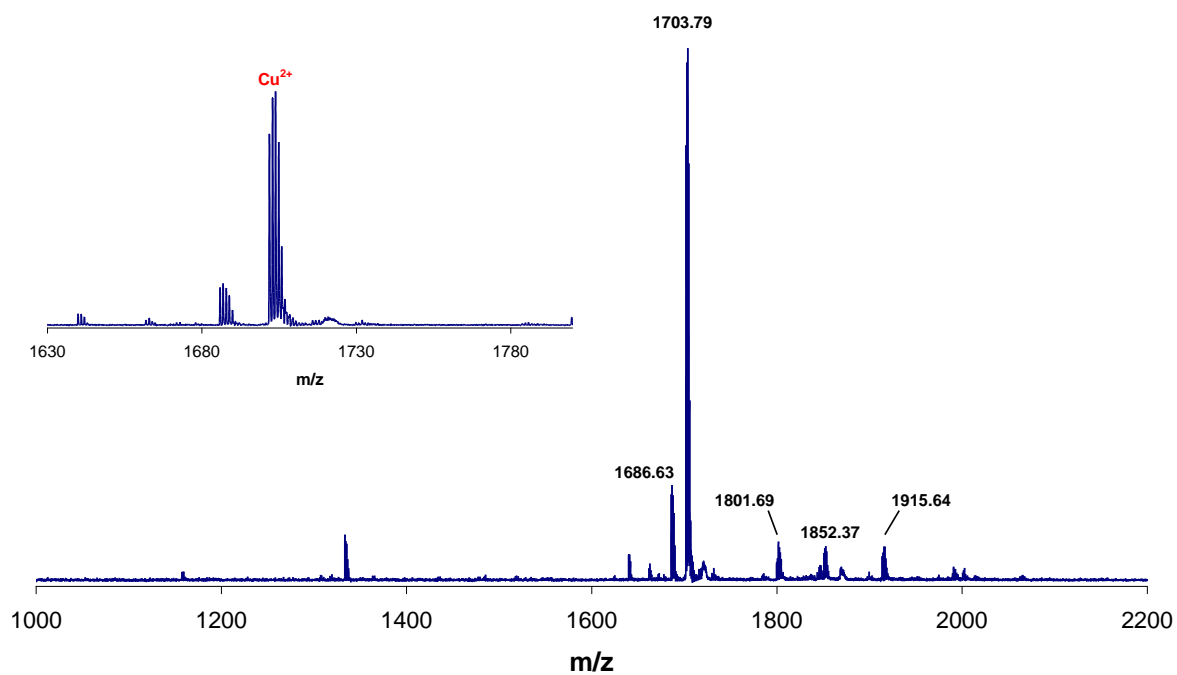


Fig.S17: MALDI-TOF spectrum of **7b** after mixing with $\text{Cu}(\text{OAc})_2$ in DCM/methanol.

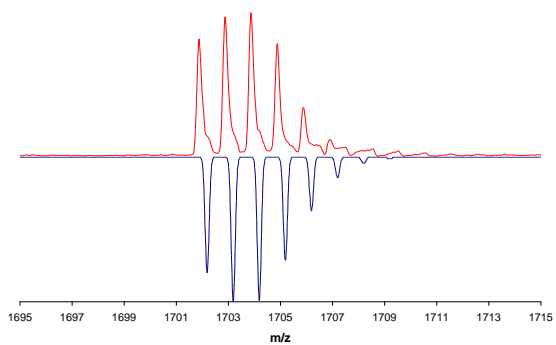


Fig.S18: Comparison between experimental (red) and theoretically calculated (blue) isotopic pattern of **7b-Cu**.

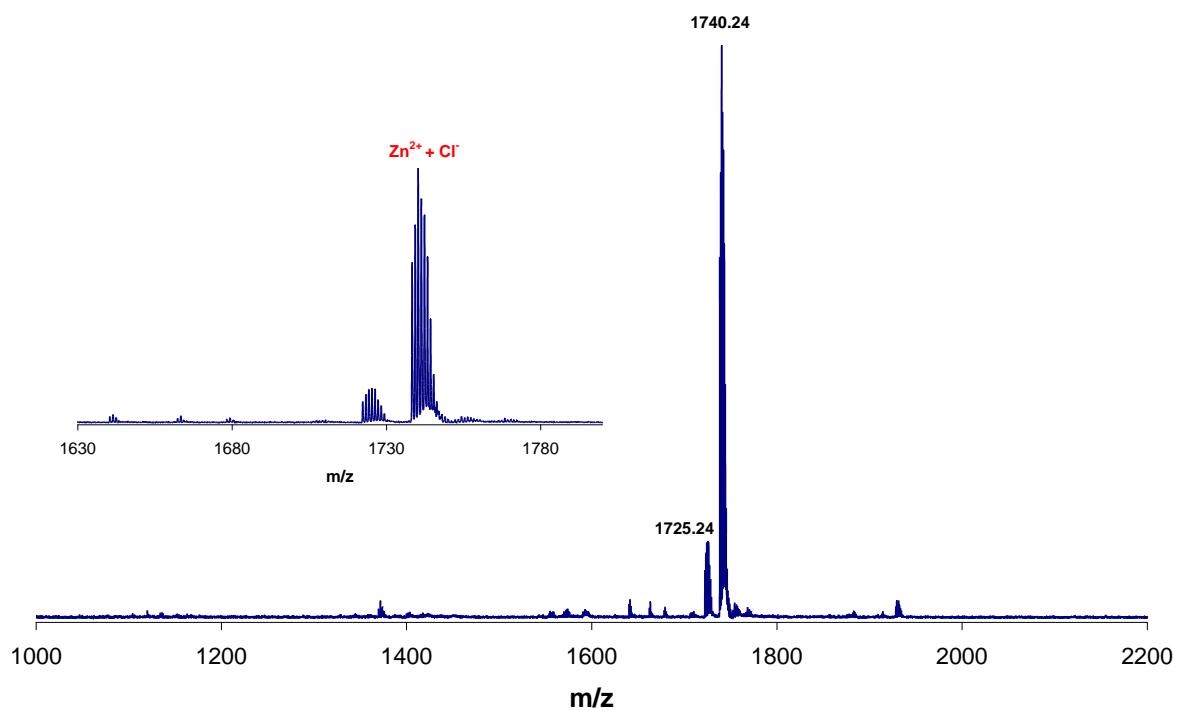


Fig.S19: MALDI-TOF spectrum of **7b** after washing with aqueous ZnCl_2 solution.

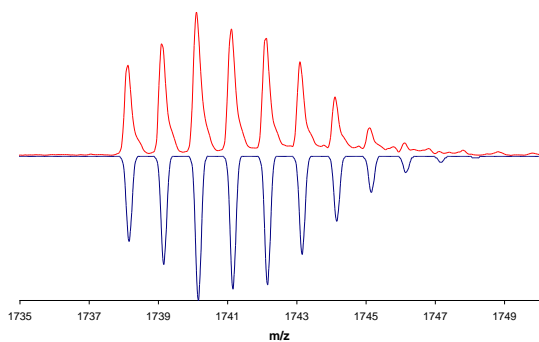


Fig.S20: Comparison between experimental (red) and theoretically calculated (blue) isotopic pattern of **7b-Zn**.

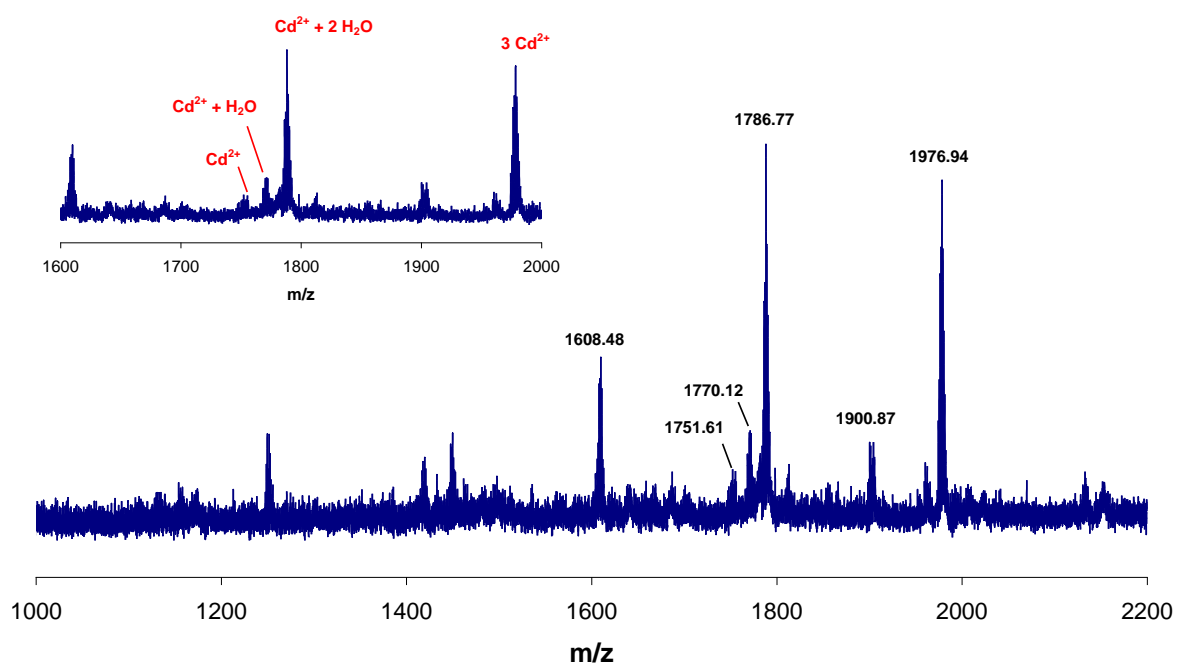


Fig.S21: MALDI-TOF spectrum of **7b** after mixing with $\text{Cd}(\text{OAc})_2 \cdot 2 \text{H}_2\text{O}$ in DCM/MeOH .

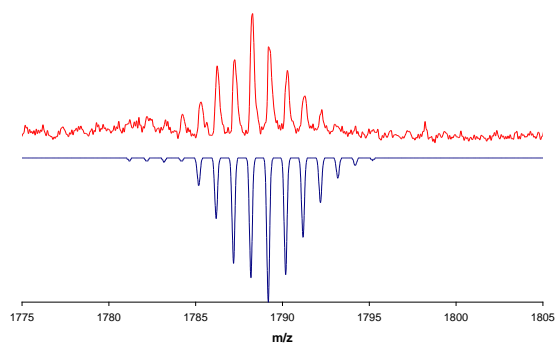


Fig.S22: Comparison between experimental (red) and theoretically calculated (blue) isotopic pattern of **7b-Cd**.

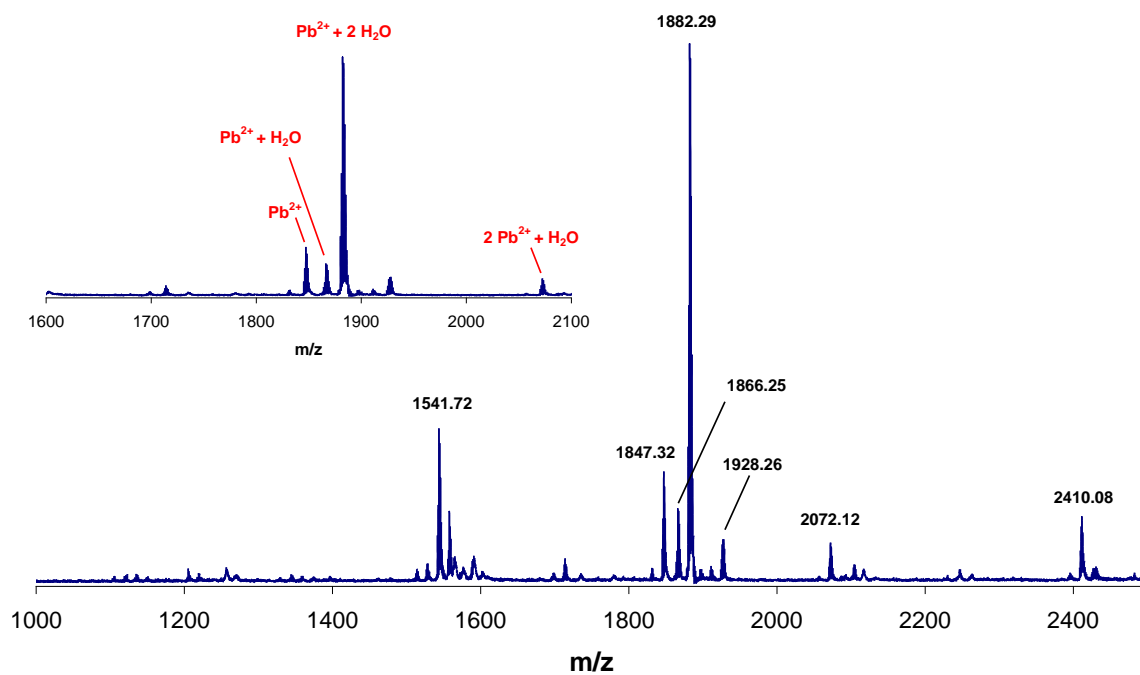


Fig.S23: MALDI-TOF spectrum of **7b** after washing with aqueous $\text{Pb}(\text{OAc})_2$ solution.

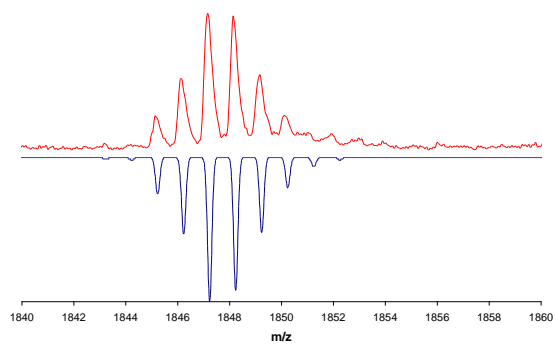


Fig.S24: Comparison between experimental (red) and theoretically calculated (blue) isotopic pattern of **7b-Pb**.

Optical Spectroscopy

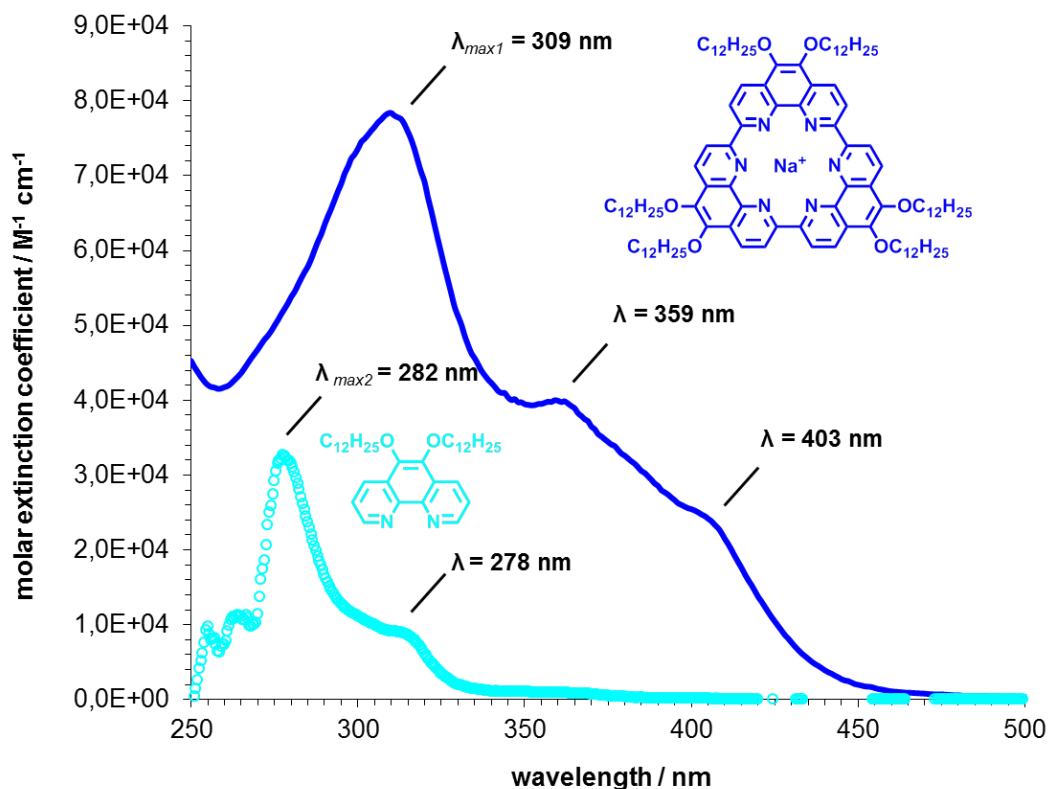


Fig.S25: UV-vis spectra of macrocycle **7b-Na** and the corresponding model compound **9** in DCM at 10^{-5} M.

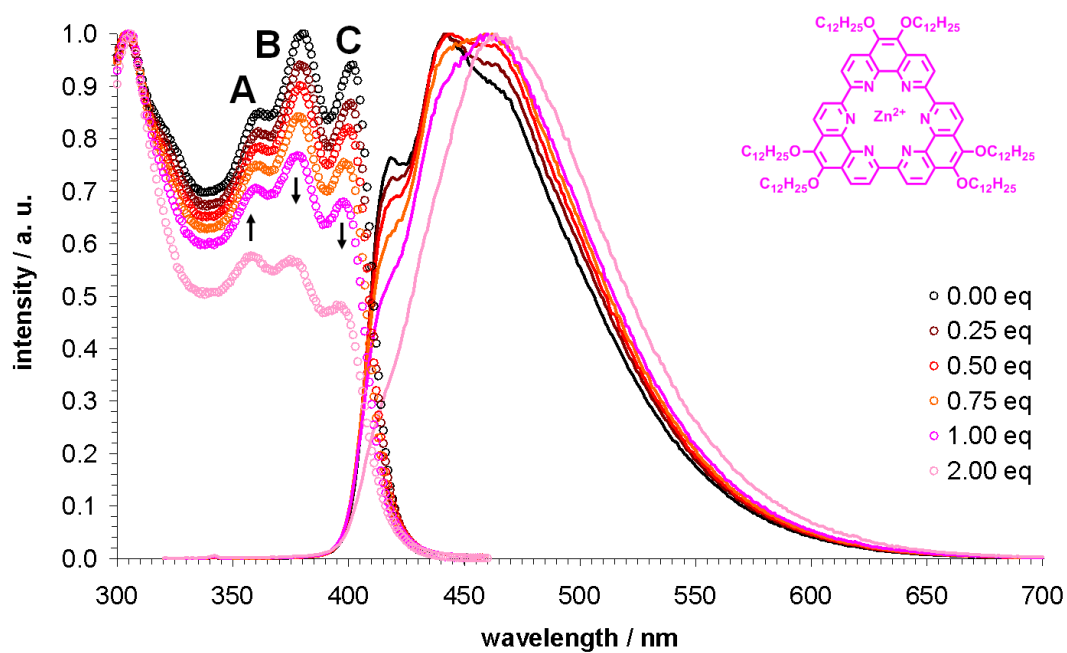


Fig.S26: Normalized fluorescence excitation and emission spectra of **7b-Na** upon titration with a zinc acetate solution (10^{-4} M) in THF at 10^{-5} M.

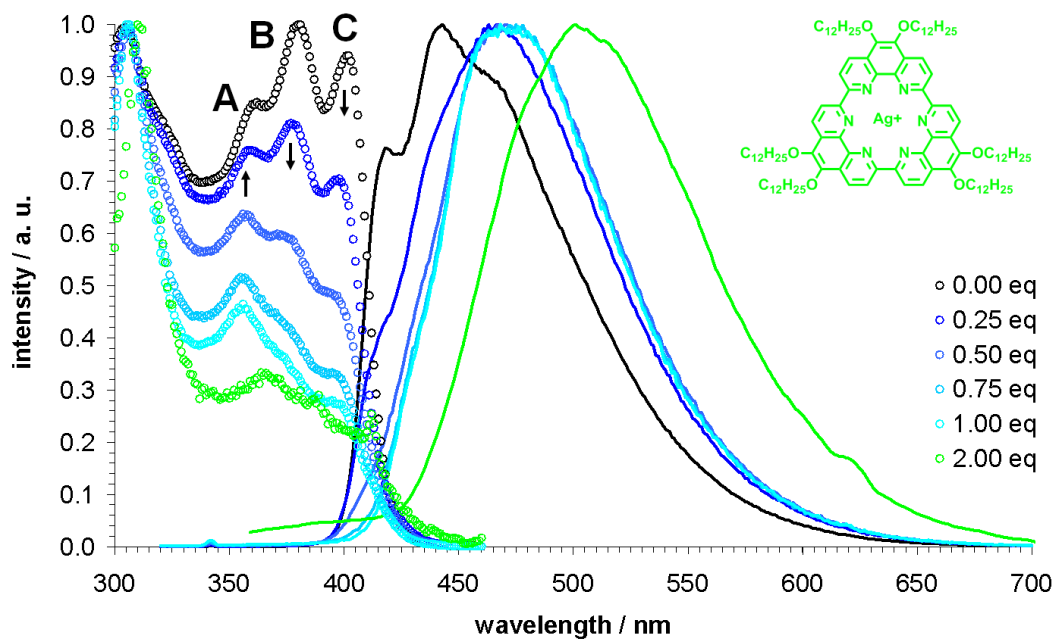


Fig.S27: Normalized fluorescence excitation and emission spectra of **7b-Na** upon titration with a silver triflate solution (10^{-4} M) in THF at 10^{-5} M.

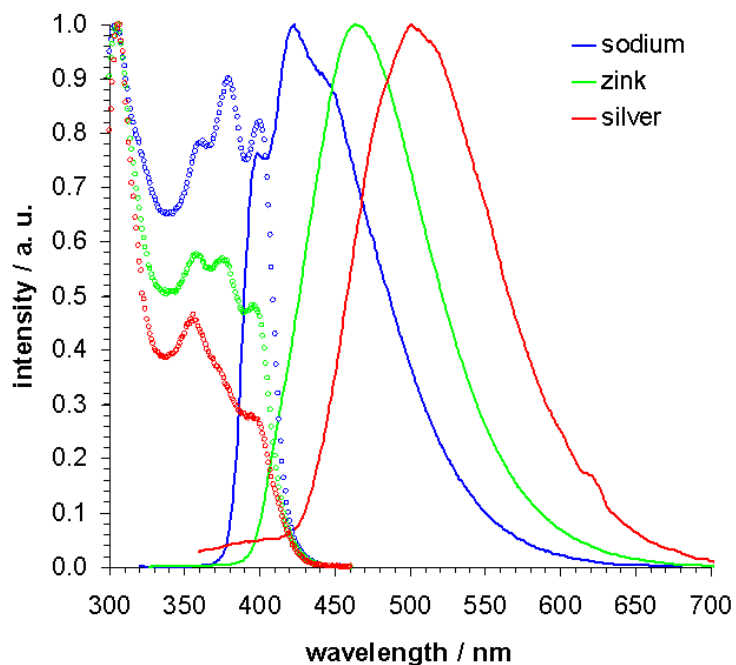


Fig.S28: Comparison of normalized fluorescence excitation and emission spectra of **7b-Na**, **7b-Zn** and **7b-Ag** in THF at 10^{-5} M.

2D-WAXS Analysis

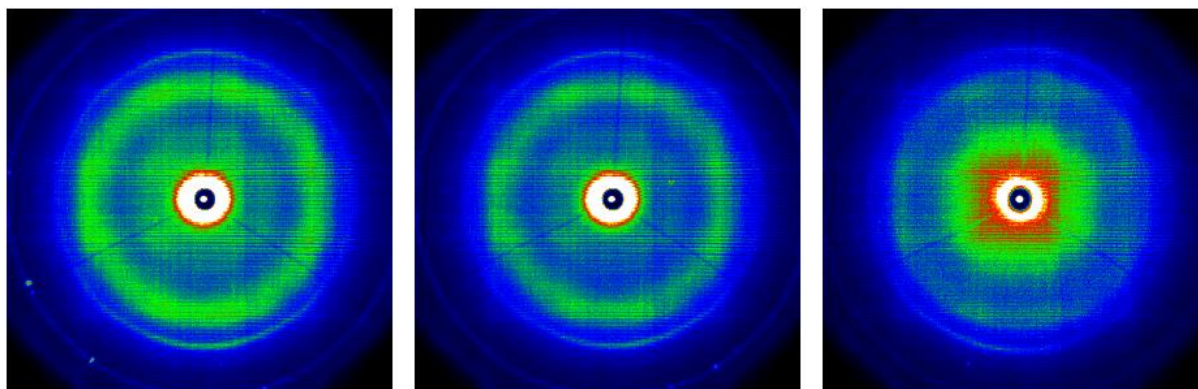


Fig.S29: 2D-WAXS patterns of an extruded fiber of **7a-Na** at 30 °C (left), 70 °C (middle) and -80 °C (right).

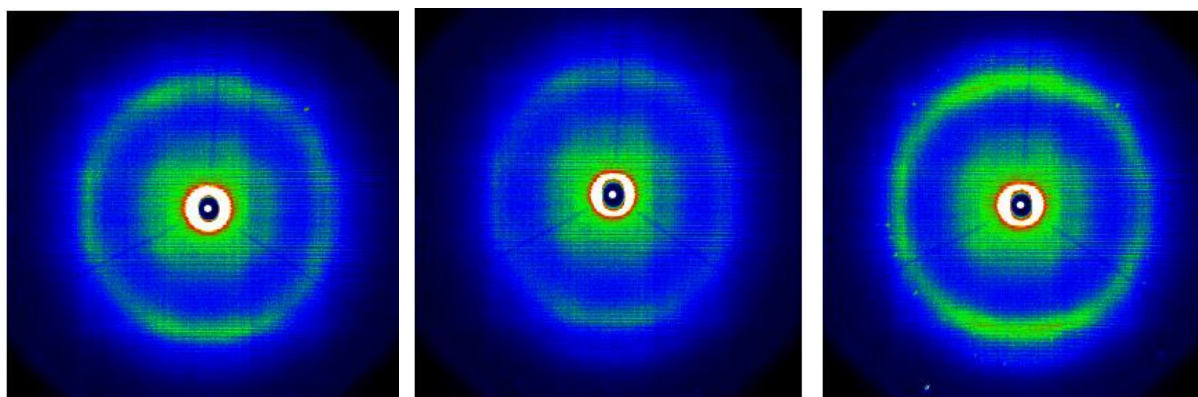


Fig.S30: 2D-WAXS patterns of an extruded fiber of **7b-Na** at 30 °C (left), 70 °C (middle) and -80 °C (right).

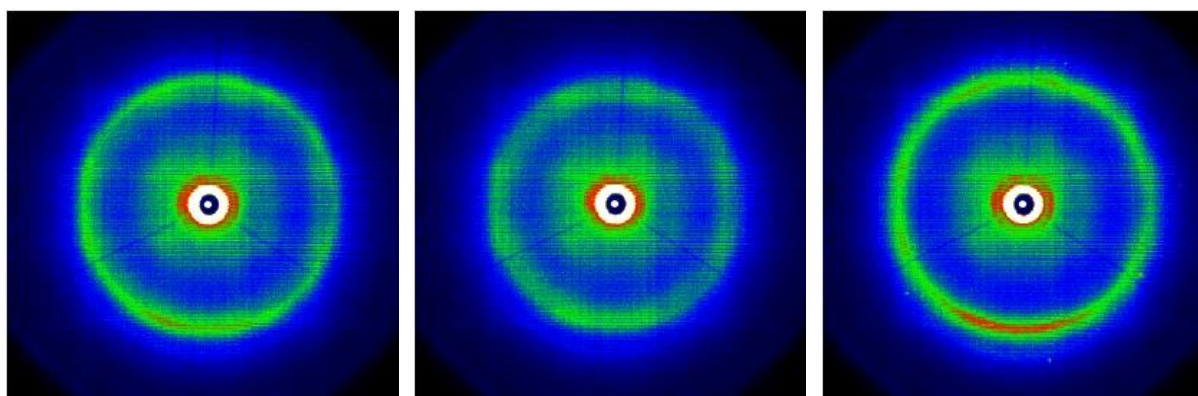


Fig.S31: 2D-WAXS patterns of an extruded fiber of **7c-Na** at 30 °C (left), 70 °C (middle) and -80 °C (right).

Computational Methods

A simplified version of the series of ligands **7a-c** was chosen for which the alkoxy side chains were replaced by R = CH₃, denoted **7d** hereafter. Complexes between the **7d** ligand and the metal guests Na⁺, Ag⁺, Pb²⁺ and Zn²⁺, were also computationally modelled. The geometries of the native ligands as well as that of the metallic complexes were optimised at the DFT level, with the BP86 functional^[8, 9] and the def2-TZVP basis set expansion.^[10] All the optimised structures present real vibrational frequencies, confirming that they correspond to true minima of the potential energy surface (PES). Geometry optimisation as well as vibrational analysis were performed with TURBOMOLE 6.2 package of programs.^[11]

An Extended Transition State (ETS)^[12-14] energy decomposition analysis combined with the Natural Orbitals for Chemical Valence (NOCV)^[15-18] method has been used to gain insight into the bonding situation between the ligand **7d** and the different metallic centres. The ETS scheme considers the molecule AB to be formed by the interaction between two fragments A and B. Then, it decomposes the interaction energy ΔE_{int} into chemically meaningful quantities:

$$\Delta E_{\text{int}} = E_{\text{AB}} - E_{\text{A}}^0 - E_{\text{B}}^0 = \Delta E_{\text{prep}} + \Delta E_{\text{elstat}} + \Delta E_{\text{Pauli}} + \Delta E_{\text{orb}}$$

Thus, the interaction energy is the difference between the energy of the complex and the energies of each fragment at their respective optimal geometry and electronic state. The first term of the partition scheme, the preparation energy (ΔE_{prep}), is the energy needed to take each fragment from their optimal geometry and electronic state (A^0 and B^0) to the geometry and electronic state they have in the molecule AB (A and B). In a second step, the prepared fragments A and B are approached together to form the final molecule AB. The term ΔE_{elstat} arises from computing the electrostatic interactions of the fragments A and B when they are close to each other. However, the total electronic wave function after applying the two previous steps (Ψ_{AB}) is merely the superposition of the electronic density of each fragment, ρ_{A} and ρ_{B} . Ψ_{AB} does not fulfil Pauli's exclusion principle nor is it optimal for the final molecule AB (Ψ_{AB}^0). First, Ψ_{AB} is antisymmetrised. The energy change on doing so corresponds to the ΔE_{Pauli} term and accounts for the electronic repulsion due to exchange. Second, this antisymmetrised wavefunction ($\Psi_{\text{AB}}^{\text{antisymm}}$) is further relaxed to Ψ_{AB}^0 , with an energy variation given by ΔE_{orb} . This last term is associated with the mixing of occupied orbitals of one fragment with unoccupied orbitals of the other fragment, as well as the mixing between occupied and unoccupied orbitals within the same fragment. The deformation density associated to this latter orbital relaxation can be diagonalised, and the eigenvalues of

that diagonalisation constitute the set of NOCVs. On the other side, each NOCV has an energy contribution to the total ΔE_{orb} . The advantage of NOCVs is that just a few of them are needed to describe the bond formation of the molecules from atoms or fragments. Thus, that small set of NOCVs will account for most of the ΔE_{orb} energy, decomposing that term into chemically meaningful electronic rearrangements.

In order to understand the nature of the bond, it is also interesting to analyse the nature of the interaction contributions of the interaction energy, given by the sum of the ΔE_{elstat} and ΔE_{orb} terms. The first term is associated to the ionic character of the bond, while the latter, to the covalent one. Thus, information about the ionic/covalent character of a bond can be inferred by analysing the participation of each term into the total interaction energy.

Minimum Energy Structure of the Cyclo-2,9-tris-1,10-phenanthroline Macrocycle

Macrocycle **7d** is not planar. The source of non-planarity is resulting from the C-C bonds holding together two neighbouring 1,10-phenanthroline units. A closed cycle formed by three 1,10-phenanthroline entities contains three of such NCCN dihedral angles, different from zero. This gives rise to two possibilities: i) all three dihedrals have the same sign, forming a structure of C_3 symmetry, or ii) a dihedral has a different sign from that of the two others, lowering the symmetry to C_2 (Fig. S32). The C_3 -structure is somewhat more planar ($\theta_{\text{NCCN}} = 18.9^\circ$) than the C_2 -one ($\theta_{\text{NCCN}} = -26.7$ and 21.3°), but the size of the cavity is rather similar for C_3 ($d(\text{N-N}) = 5.611 \text{ \AA}$) and C_2 ($d(\text{N-N}) = 5.558$ and 5.614 \AA) (compare the overlay of both structures in Fig. S32).

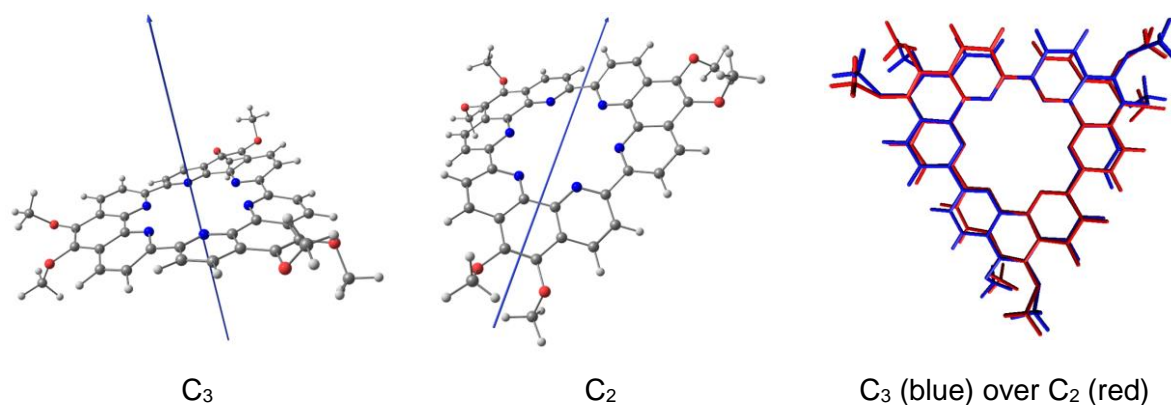


Fig.S32: DFT optimized geometry of **7d** constraint to the C_3 and C_2 symmetry point groups. The blue line represents the C_n symmetry axes.

The C₂ ligand is slightly more stable, lying 1 kcal mol⁻¹ lower in energy than the C₃ conformer. More importantly, however, is the different number of isomers of each structure, or degeneracy. With three NCCN dihedrals, there are three different possible combinations of one positive and two negative (or two negative and one positive) NCCN dihedrals. However, there is only one possible combination having three positive (or three negative) dihedrals. Therefore, the C₂-structure has a degeneracy that is three times larger than the C₃ conformer. Indeed, according to a Boltzmann distribution, the former isomer should be present in 94 % at 298 K given the energy and degeneracy differences accounted for. Interestingly, such an alternation of the sign of the dihedral angle has been already reported in the X-ray crystal structures of related torands.^[19]

Geometrical Distortion of the Ligand upon Guest Inclusion

The results from MALDI-TOF spectrometry divide the guest cations investigated in this work in three groups: i) Na⁺, ii) Ag⁺ and Cu²⁺, forming 1:1 adducts, and iii) Pb²⁺, Cd²⁺ and Zn²⁺, with counterions participating in the complex formation. To better understand the different bonding schemes of each group, a representative cation of each of them, namely: Na⁺, Ag⁺ and Zn²⁺, has been chosen. From the last group, Pb²⁺ is additionally considered, as it is not a transition metal and can display different bonding schemes.

The adduct formed upon chelation with Na⁺, Ag⁺ and Pb²⁺ preserve the C₂ symmetry of the native ligand, with the guest staying in the center of the cavity. Indeed, chelation produces little geometrical distortion on the cyclic ligand (Table S1). When comparing the geometry of the native macrocycle to the one of these three complexes it is found that they overlap rather well (compare Fig. S33a). The root mean square deviation (RMSD) for the overlaid structures of the adducts with Na⁺, Ag⁺ and Pb²⁺ onto the geometry of the bare ligand yields values of 0.050, 0.0778 and 0.1038 Å, respectively.

Table S1: Comparison of the two N-N distances (in Å) defining the size of the cavity within the macrocycle and the CNNC dihedrals (in °) responsible for the non-planarity of the ligand.

	d(N-N)	d'(N-N)	θ _{NCCN}	θ' _{NCCN}	d _{max} (M-N)	d _{min} (M-N)
Native	5.614	5.574	26.7	21.3		
Na ⁺	5.555	5.524	20.1	17.5	2.778	2.758
Ag ⁺	5.533	5.491	22.1	18.1	2.784	2.716
Pb ²⁺	5.573	5.550	16.1	15.0	2.786	2.771

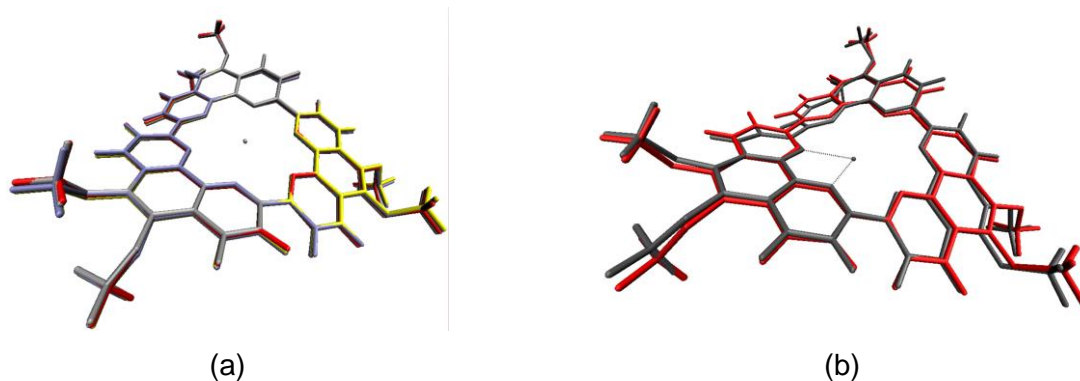


Fig.S33: a) Superposition of the structures of the native cyclo-2,9-tris-1,10-phenanthroline **7d** (red) and upon chelation with Na⁺ (**7d-Na**, yellow), Ag⁺ (**7d-Ag**, silver) and Pb²⁺ (**7d-Pb**, purple). **b)** Superposition of the structures of the native cyclo-2,9-tris-1,10-phenanthroline (**7d**, red) and the complex with Zn²⁺ (**7d-Zn**, grey).

The deformation of the ligand is, however, significantly larger upon complexation with Zn²⁺. In this scenario, the complex loses its symmetry; the metal leaves the center of the cavity and establishes specific interactions with two particular nitrogen atoms (compare Fig. S33b). This is possible due to the small size of the Zn²⁺ cation (0.88 Å), which is actually the smallest cation of the investigated series (1.16 Å, 1.29 Å and 1.33 Å for Na⁺, Ag⁺ and Pb²⁺, respectively).

Placing the Zn²⁺ cation between each possible pair of nitrogen atoms, the six initial structures converged to basically three different minima degenerate in energy (energy difference < 0.2 kcal mol⁻¹), whose geometries can be considered as practically equivalent (see Fig. S34).

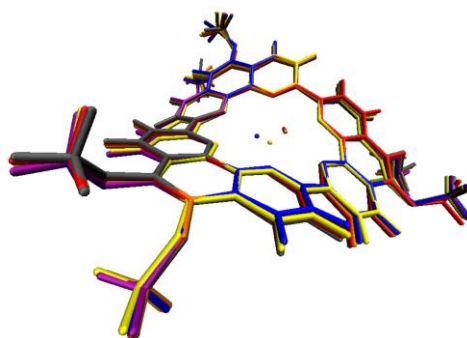


Fig.S34: Superposition of all the optimized structures for the **7d-Zn** adduct.

Table S2 summarizes the most relevant geometrical parameters of the three different isomers, and compares them to the structure of the native ligand. The net effect of the complexation with Zn²⁺ is a closing of the cavity and larger planarity of the ligand.

Table S2: Geometrical parameters for three conformers of the **7d-Zn** adduct, corresponding to the colors yellow (1), blue (2) and red (3) of Figure S34.

	d(N-N)	d'(N-N)	d''(N-N)	θ_{NCCN}	θ'_{NCCN}	θ''_{NCCN}	$d_{\text{max}}(\text{M-N})$	$d_{\text{min}}(\text{M-N})$	$d'_{\text{min}}(\text{M-N})$
Native	5.614	5.574	5.574	-26.7	-26.7	21.3			
Zn ²⁺ (1)	5.520	5.3224	5.267	-18.8	-17.9	16.7	3.489	2.077	2.322
Zn ²⁺ (2)	5.599	5.314	5.276	-19.1	-13.6	22.4	3.523	2.081	2.246
Zn ²⁺ (3)	5.607	5.294	5.274	-20.1	-10.4	22.8	3.531	2.077	2.318

Analysis of the Metal-Ligand Bond

On each four complexes, an ETS-NOCV energy decomposition analysis has been performed in order to get better insight into the bonding state between the cationic guest and the ligand. Table S3 summarizes the results of the decomposition analysis, each individual case being discussed thereupon.

Table S3: Energy decomposition Analysis (EDA) of the M-ligand adducts (M = Na⁺, Ag⁺, Pb²⁺ and Zn²⁺). Below the E_{elect} and E_{orb} terms its relative contribution to the total bonding interactions ($E_{\text{int}} + E_{\text{Pauli}}$) is displayed.

All values are in kcal mol⁻¹.

	Na ⁺	Ag ⁺	Pb ²⁺	Zn ²⁺
E_{int}	-115.12	-145.94	-304.26	-424.23
E_{Pauli}	13.53	41.26	95.78	62.65
E_{Elec}	-92.20	-119.69	-214.55	-237.98
	(72%)	(64%)	(54%)	(49%)
E_{orb}	-36.45	-67.51	-185.49	-248.89
	(28%)	(36%)	(46%)	(51%)

7d-Na

Table S3 shows that for this system the interaction between metal and ligand is basically electrostatic, 72% of total bonding interactions. The remaining 28% corresponds to orbital interactions. The deformation matrix associated has been decomposed and its main and predominant component is depicted in Fig. S35. This figure (as well as the related figures hereafter) makes use of the following color code: Red lobes correspond to regions where the electronic density decreases and blue ones, where it increases. Hence, Figure S35 illustrates a charge donation from all nitrogen lone pairs to the metal. This is mainly associated to a

polarization of the electronic density of the ligand instead of a real covalent bond between ligand and metal. Consequently, for this instance, the bond is mainly due to electrostatic interactions, which are further stabilized by a polarization of the electronic density of the ligand.

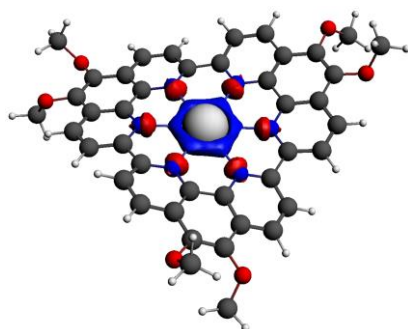


Fig. S35: Natural orbital of the deformation density with highest eigenvalue for the complex **7d-Na**.

7d-Ag

In comparison to Na^+ , the ligand-metal interaction has a greater covalent character in the case of Ag^+ . In absolute terms, the covalent interactions have increased by ca. 31 kcal mol^{-1} . Fig. S36 reveals that most of this increase is originating from a ligand-to-metal charge transfer $\sigma(\text{N}) \rightarrow 5s(\text{Ag})$, contributing 21 kcal mol^{-1} to the bonding. As a minor effect, there are two orbitals, degenerate in energy, representing polarizations of the lone pairs of the ligand, amounting for further 12 kcal mol^{-1} . Summing up, the greater ligand-metal interaction energy of **7d-Ag** presents a greater ligand-metal interaction energy than **7d-Na** due to the formation of a covalent bond, $\sigma(\text{N}) \rightarrow 5s(\text{Ag})$. This is possible thanks to the accessible empty s orbitals of Ag^+ .

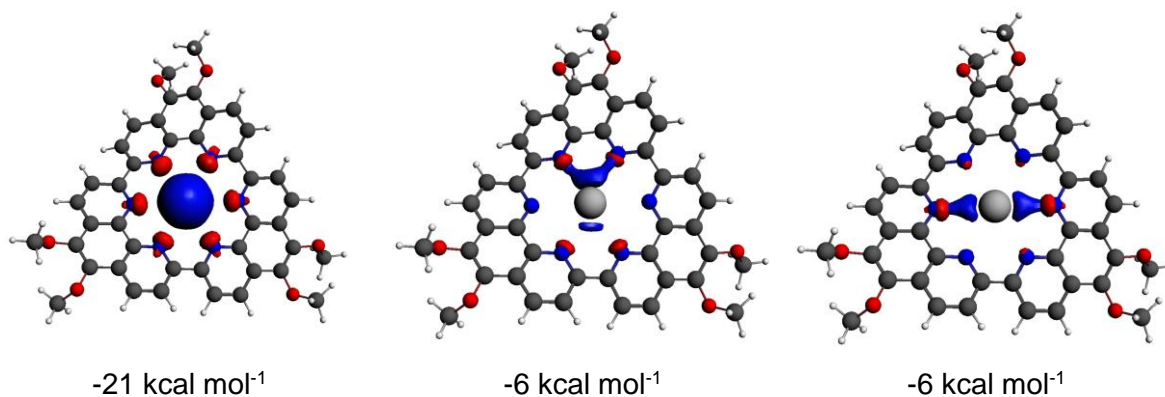


Fig. S36: Natural orbitals of the deformation density with the three highest eigenvalues for the **7d-Ag** complex. Below each orbital is shown the associated stabilization energy.

7d-Pb

The E_{elec} term is ca. $100 \text{ kcal mol}^{-1}$ larger than for previous metals. This is to be expected as Pb^{2+} is doubly charged while Na^+ or Ag^+ are monocations. The covalent component of the bonding increases even more resulting in a larger relative contribution to the total attractive interactions. Thus, the ligand-metal interaction has also a stronger covalent component than in Na^+ or Ag^+ . This is the case since for **7d-Pb** there are not one but two charge transfers from the nitrogen lone pairs to the two empty $6p$ orbitals of Pb^{2+} contained in the plane of the ligand (see Fig. S37). This two $\sigma(\text{N}) \rightarrow 6p(\text{Ag})$ donations, amounting to 74 kcal mol^{-1} in total, account for most of the increase of the covalent component of the ligand-metal bond. The ETS-NOCV analysis shows that the ligand **7d** binds to Pb^{2+} more strongly than to Na^+ and Ag^+ due to i) a stronger electrostatic interaction arising from the larger charge of the cation which are complemented by ii) stronger covalent interactions arising from two $\sigma(\text{N}) \rightarrow 6p(\text{Ag})$ charge donations.

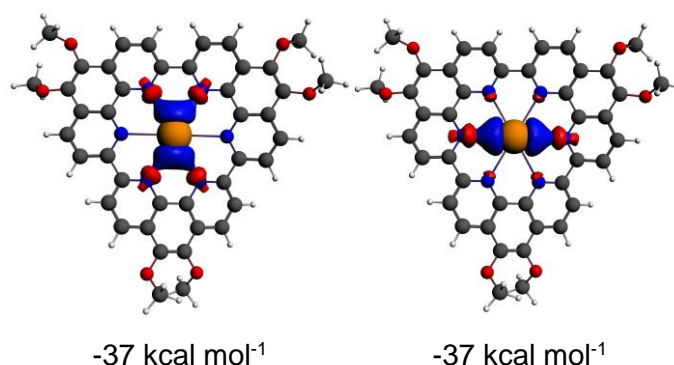


Fig. S37: Natural orbitals of the deformation density with the two highest eigenvalues for **7d-Pb**. Below each orbital is shown the associated stabilization energy.

7d-Zn

Again, this metal presents an ionic component being ca. $100 \text{ kcal mol}^{-1}$ larger than that for monocationic metal species. The covalent component undergoes still a larger increase. The interactions between guest and ligand of the **7d-Zn** complex have the highest degree of covalency for the series studied. Figure S38 represents the dominant natural orbitals into which the deformation density matrix can be decomposed.

According to this figure, the main component of the covalent bonding corresponds to a charge transfer $\sigma(\text{N}) \rightarrow 3s(\text{Zn})$, amounting for 71 kcal mol^{-1} . This charge transfer is significantly larger than the equivalent one found in **7d-Ag** (amounting for 21 kcal mol^{-1}). Indeed, the shorter M-N distances in the Zn^{2+} adduct renders possible a better orbital overlap

between metal and ligand. Additionally, there are some additional charge transfers from the ligand to the metal representing some π component of the bonding. Further N-Zn bonds, where the p orbitals of Zn^{2+} are involved, can be also recognized.

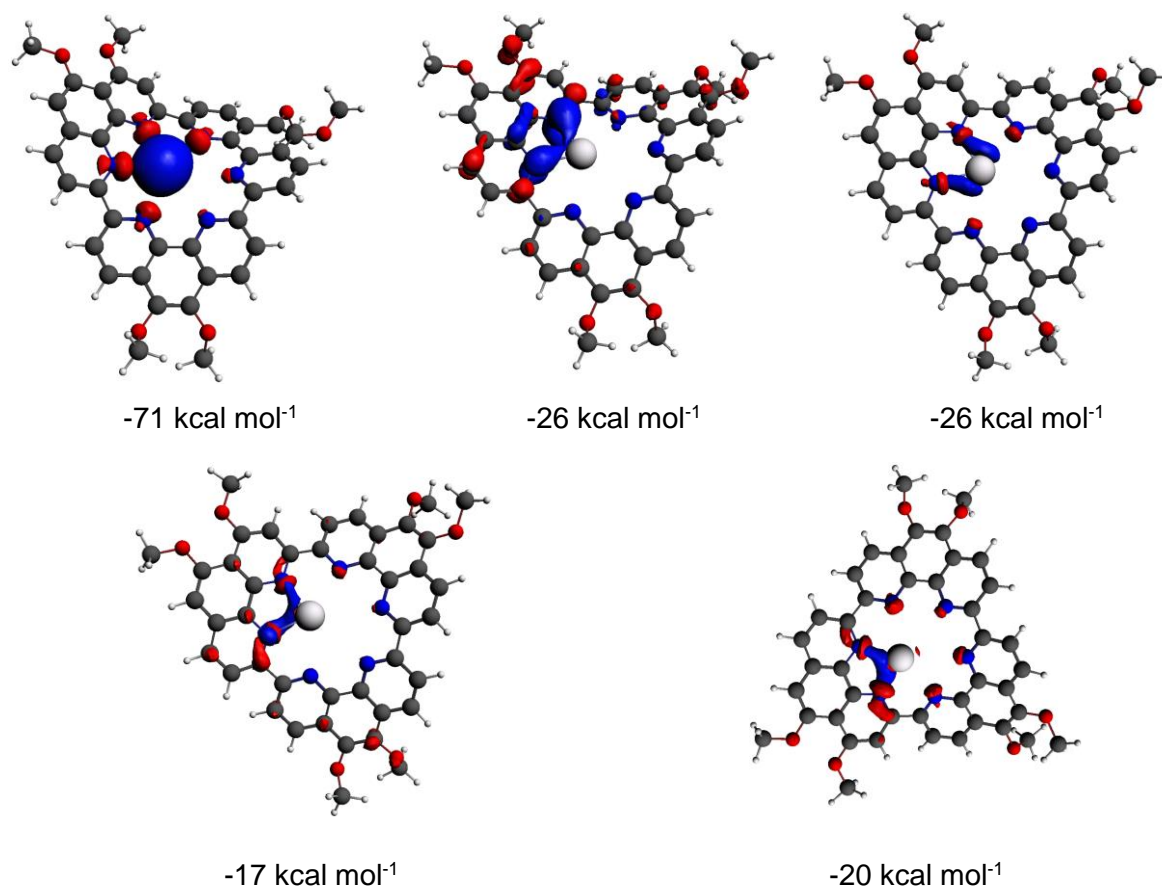


Fig. S38: Natural orbitals of the deformation density with the five highest eigenvalues for **7d-Zn**.
Below each orbital is shown the associated stabilization energy.

In summary, the small size of the Zn^{2+} cation allows it to leave the center of the cavity and approach specific nitrogen atoms of the ligand cavity. This yields an effective overlap between the orbitals of metal and ligand and the strongest covalent bonds of the investigated series. The large charge of the cation and the proximity to the ligand produces also to the strongest electrostatic interactions between metal and ligand. However, for this complex the covalent component is very important and accounts for half of the attractive interactions of the bond.

Scanning Tunneling Microscopy

STM experiments were carried out using a PicoSPM (Agilent) operating in the constant-current mode with the tip immersed in the supernatant liquid at room temperature. STM tips were prepared by mechanical cutting from Pt/Ir wire (80%/20%, diameter 0.2 mm). Prior to imaging, compound **7b** was dissolved (concentration = $5.5 \cdot 10^{-4}$ M) in 1-phenyloctane (Aldrich, 98%) and a drop of this solution was applied onto a freshly cleaved surface of highly oriented pyrolytic graphite (HOPG, grade ZYB, Advanced Ceramics Inc., Cleveland, USA). For analysis purposes, recording of a monolayer image was followed by imaging the graphite substrate underneath it under the same experimental conditions, except for lowering the bias. The images were corrected for drift via Scanning Probe Image Processor (SPIP) software (Image Metrology ApS), using the recorded graphite images for calibration purposes, allowing a more accurate unit cell determination. The imaging parameters are indicated in the figure caption: tunneling current (I_t), and sample bias (V_t).

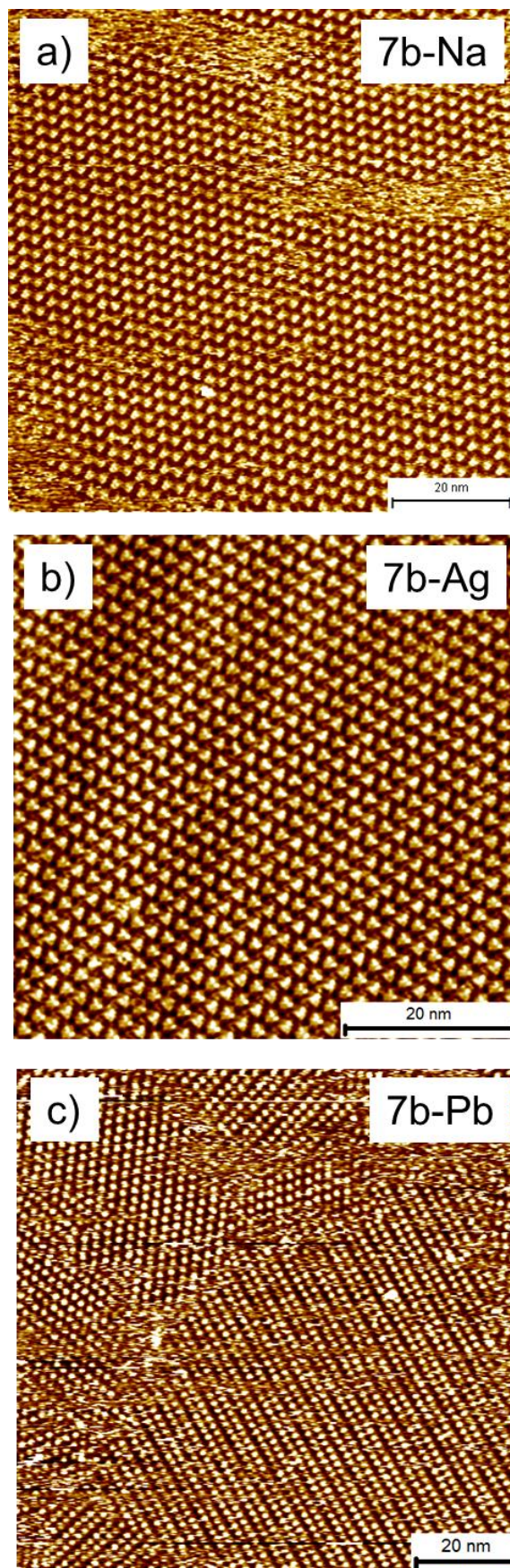


Fig. S39: Large-scale STM images of the macrocycles showing well-ordered 2D supramolecular assemblies formed at the 1-phenyloctane/HOPG interface. The images were obtained using tunneling conditions that vary between $V_{\text{bias}} = -800 \text{ mV}$ to -1.1 V and $I_{\text{set}} = 100 \text{ pA}$ to 160 pA .

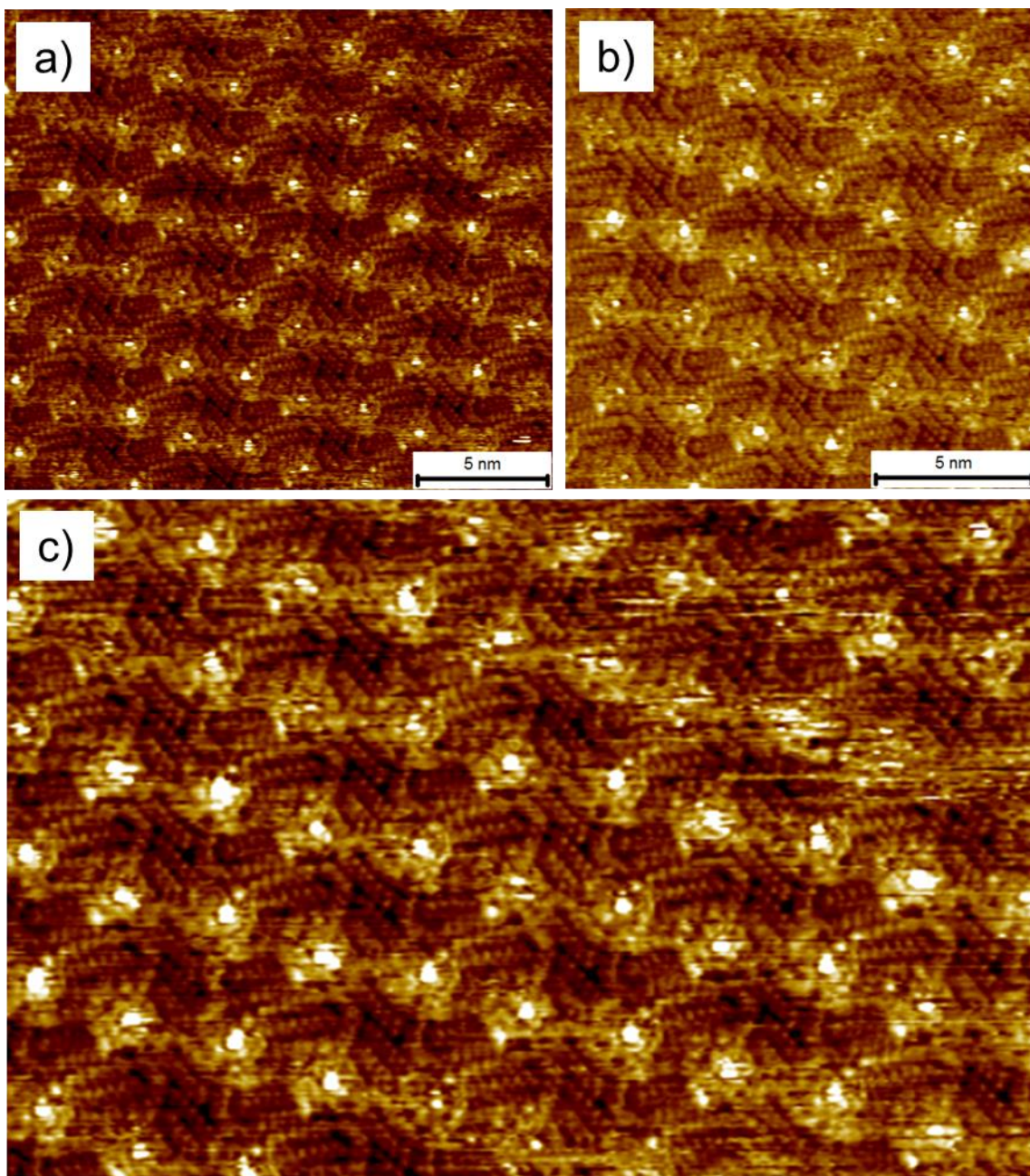


Fig. S40: Additional STM images showing the peculiar STM contrast of the macrocycle cavity when the Pb^{2+} cation is present. The images were obtained using different tips, in different experimental sessions and the tunneling conditions vary between $V_{\text{bias}} = -800 \text{ mV}$ to -1.1 V and $I_{\text{set}} = 100 \text{ pA}$ to 160 pA .

Electron Microscopy

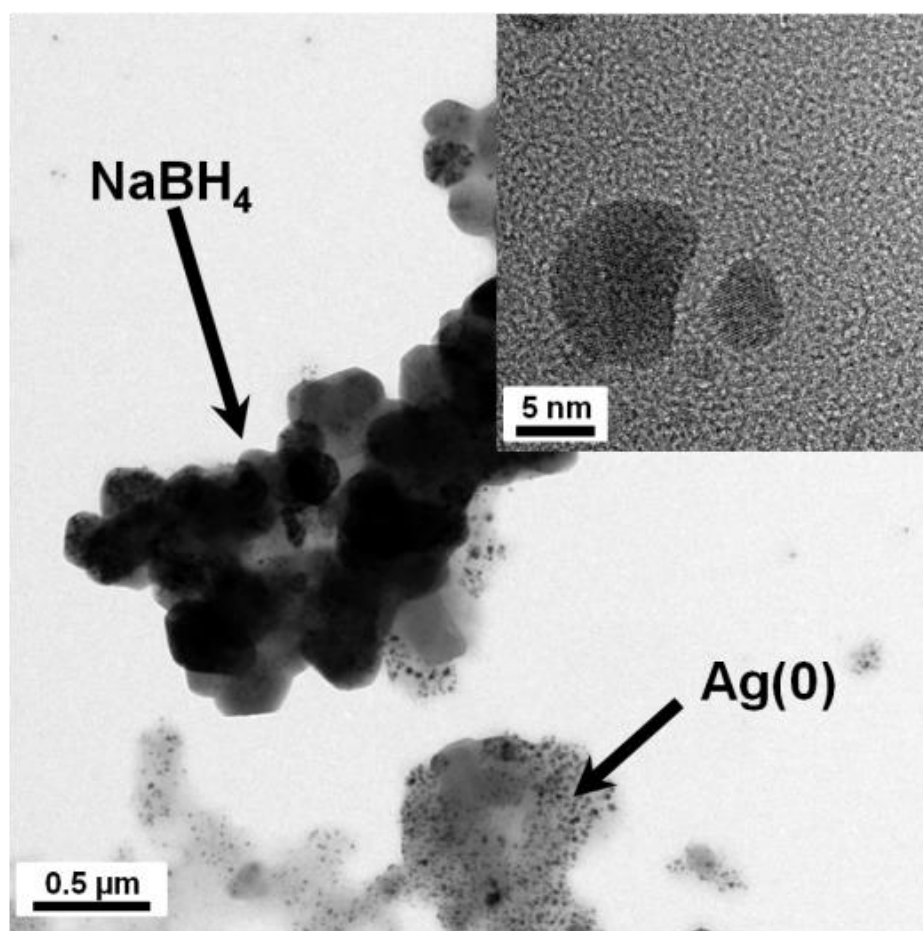


Fig. S41: The reduction of **7b-Ag** with sodium borohydride: TEM micrograph of the resulting precipitate. The inset shows a magnification of individual silver nanoparticles.

References

- [1] M. Yamada, Y. Nakamura, S. Kuroda and I. Shima, *Bull. Chem. Soc. Jpn.* **1990**, *63*, 2710-2712.
- [2] M. Yamada, Y. Tanaka, Y. Yoshimoto, S. Kuroda and I. Shima, *Bull. Chem. Soc. Jpn.* **1992**, *65*, 1006-1011.
- [3] T. Yamamoto, S. Wakabayashi and K. Osakada, *J. Organomet. Chem.* **1992**, *428*, 223-237.
- [4] T. Yamamoto, T. Maruyama, Z. H. Zhou, T. Ito, T. Fukuda, Y. Yoneda, F. Begum, T. Ikeda and S. Sasaki, *J. Am. Chem. Soc.* **1994**, *116*, 4832-4845.
- [5] G. W. Parshall, *J. Am. Chem. Soc.* **1974**, *96*, 2360-2366.
- [6] T. Yamamoto, T. Kohara and A. Yamamoto, *Bull. Chem. Soc. Jpn.* **1981**, *54*, 1720-1726.
- [7] Z. H. Zhou and T. Yamamoto, *J. Organomet. Chem.* **1991**, *414*, 119-127.
- [8] A. D. Becke, *Phys. Rev. A* **1988**, *38*, 3098-3100.
- [9] J. P. Perdew, *Phys Rev B Condens Matter* **1986**, *34*, 7406.
- [10] F. Weigend and R. Ahlrichs, *Phys. Chem. Chem. Phys.* **2005**, *7*, 3297-3305.
- [11] TURBOMOLE V6.2 2010; a development of University of Karlsruhe and Forschungszentrum Karlsruhe GmbH, TURBOMOLE GmbH, since 2007; available from <http://www.turbomole.com>, Karlsruhe, Deutschland.
- [12] T. Ziegler and A. Rauk, *Theor. Chim. Acta* **1977**, *46*, 1-10.
- [13] T. Ziegler and A. Rauk, *Inorg. Chem.* **1979**, *18*, 1558-1565.
- [14] T. Ziegler and A. Rauk, *Inorg. Chem.* **1979**, *18*, 1755-1759.
- [15] A. Michalak, R. L. DeKock and T. Ziegler, *J. Phys. Chem. A* **2008**, *112*, 7256-7263.
- [16] M. Mitoraj and A. Michalak, *Organometallics* **2007**, *26*, 6576-6580.
- [17] M. P. Mitoraj, A. Michalak and T. Ziegler, *J. Chem. Theory Comput.* **2009**, *5*, 962-975.
- [18] M. P. Mitoraj, H. Zhu, A. Michalak and T. Ziegler, *Int. J. Quantum Chem.* **2009**, *109*, 3379-3386.
- [19] T. W. Bell, P. J. Cragg, A. Firestone and D.-I. A. Kwok, *Angew. Chem. Int. Ed.* **1992**, *31*, 345-347.